Remyelination protects neurons from DLK-mediated neurodegeneration

Highlights

- Deletion of *Myrf* from both OLs and OPCs causes demyelination and blocks remyelination
- Remyelination protects neurons from axonal damage and apoptosis
- MAPK and c-Jun phosphorylation are increased following remyelination failure
- DLK is necessary for the apoptosis of chronically demyelinated neurons

Authors/affiliations

Greg J Duncan[1*], Samantha D Ingram[1], Katie Emberley[1], Jo Hill[2], Christian Cordano[3,4,5], Ahmed Abdelhak[3], Michael McCane[1], Nora Jabassini[3], Kirtana Ananth[3], Skylar J. Ferrara[2], Brittany Stedelin[1], Sue A. Aicher[2], Thomas Scanlan[2], Trent A Watkins[6], Anusha Mishra[1], Jonathan Nelson[7], Ari J. Green[3], Ben Emery[1,8*]

[1] Department of Neurology, Jungers Center for Neurosciences Research, Oregon Health & Science University, Portland, OR, 97239, USA

[2] Department of Chemical Physiology and Biochemistry, Oregon Health & Science University, Portland, OR, 97239, USA

[3] Weill Institute for Neurosciences, Department of Neurology, University of California San Francisco, San Francisco, CA, 94158, USA.

[4] Department of Neurology, Rehabilitation, Ophthalmology, Genetics, Maternal and Child Health (DINOGMI), University of Genoa, Italy

[5] IRCCS Ospedale Policlinico San Martino, Genova

[6] Division of Neuroimmunology and Glial Biology, Department of Neurology, University of California-San Francisco, San Francisco, CA 94158

[7] Division of Nephrology and Hypertension, School of Medicine, Oregon Health & Science University, Portland, OR, 97239, USA

[8] Lead author

[*] Co-corresponding authors

Correspondence: duncangr@ohsu.edu, emeryb@ohsu.edu, X (Twitter) @GregDuncs

Keywords

Myelin; remyelination; Myrf; oligodendrocyte; neurodegeneration; multiple sclerosis; c-Jun; MAPK; DLK; microglia,

Summary

Multiple sclerosis is characterized by inflammatory demyelination and limited remyelination in most individuals. Chronic demyelination is theorized to contribute to neurodegeneration and drive progressive disability. Here, we describe two rodent models of genetic demyelination, one characterized by effective remyelination, and the other by a failure to remyelinate. By comparing these two models, we find that remyelination helps protect axons from damage and neurons from apoptosis, improves conduction and promotes functional recovery. Chronic demyelination of neurons leads to activation of the mitogen-associated protein kinase (MAPK) stress pathway downstream of dual leucine zipper kinase (DLK), cumulating in phosphorylation of c-Jun. Both pharmacological inhibition and CRISPR/Cas9-mediated disruption of DLK block c-Jun phosphorylation and apoptosis of demyelinated neurons. These findings provide direct experimental evidence that remyelination is neuroprotective and identify DLK inhibition as a potential therapeutic strategy to protect chronically demyelinated neurons.

Introduction

Remyelination is the regenerative process by which new myelin sheaths are produced in the CNS, typically via the differentiation of oligodendrocytes (OLs) from oligodendrocyte precursor cells (OPCs)[1-3], or to a limited extent by OLs that survive the demyelinating insult[4-8]. In the inflammatory demyelinating disease multiple sclerosis (MS), remyelination is often incomplete, resulting in chronic demyelination of axons[9-12]. Chronic demyelination and the associated loss of OLs deprive neurons of crucial metabolic and trophic support, which is hypothesized to leave them vulnerable to subsequent degeneration[13-17]. With disease chronicity, there is a progressive loss of neurons and their synapses in MS which drives permanent disability[18-21]. While several studies have found an association between remyelination efficiency and neurodegeneration in MS[22-24], there is a paucity of direct experimental evidence demonstrating that remyelination failure triggers neurodegeneration. At this time, no study has genetically targeted the oligodendrocyte lineage to induce demyelination and block subsequent remyelination to determine if remyelination failure is causative of neurodegeneration. Additionally, blocking remyelination would model the stress neurons are placed under during chronic demyelination and may reveal mechanistic insights into the intraneuronal changes that culminate in neurodegeneration.

Axonal damage occurs coincident with demyelination in MS[21,25-28], but it remains unclear to what extent demyelination-induced damage to the axon causes the loss of the neuronal soma. Following traumatic axonal damage or during trophic factor withdrawal, the MAP3K DLK acts as a sensor of axonal stress and activates downstream MAPKs[29,30]. These downstream MAPKs include MKK4/7 and JNK[31-35] and constitute a retrograde signaling cascade that ultimately results in the phosphorylation and activation of the transcription factor c-Jun[30,36-38]. DLK-mediated phosphorylation of c-Jun is associated with apoptosis and loss of neurons in several neurodegenerative diseases[36]. However, it remains unclear whether DLK drives neuronal loss in demyelinating disease.

In this study, we compare two rodent models of genetic demyelination which feature either successful or impaired remyelination, with the aim of understanding if remyelination failure causes greater neurodegeneration. Both lines induce demyelination by inactivating the Myelin

Regulatory Factor (*Myrf*) gene, which encodes a transcription factor essential for OL identity and myelin protein expression from OLs[39-42]. Inducible ablation of *Myrf* from OLs in adult mice leads to CNS-wide demyelination within 10 weeks followed by successful remyelination by 20 weeks. In contrast, when the deletion of *Myrf* is extend to OPCs along with OLs, OL differentiation is stalled and there is a near-complete block of subsequent remyelination. By contrasting these two rodent models, we find direct experimental evidence that successful remyelination is associated with protection from axonal damage and neuronal apoptosis. Chronic demyelination culminates in phosphorylation of the MAPKs JNK and MKK4, c-Jun phosphorylation and apoptosis of retinal ganglion cells (RGCs). Both pharmacological inhibition or genetic knockout of DLK are sufficient to block phosphorylation of c-Jun and RGC apoptosis, indicating that DLK is an upstream MAP3K necessary for chronic demyelination-induced neurodegeneration. Together, we provide direct experimental evidence that remyelination protects neurons from degeneration induced by the activation of DLK-mediated signaling, and inhibiting DLK is sufficient to preserve chronically demyelinated neurons.

Results

Myrf knockout from both OPCs and mature OLs results in genetic demyelination with little remyelination.

A rodent model in which remyelination is inhibited in a cell-selective manner would permit an understanding of the extent and mechanisms by which prolonged demyelination damages neurons. To develop a mouse model of remyelination failure, we leveraged our previous work on the transcription factor *Myrf*. *Myrf* is essential for myelin gene transcription[39-42], and its deletion from mature OLs in the adult mouse using the Plp1-CreERT mouse (Myrf$^{fl/fl}$ Plp1 CreERT; hereto referred to as Myrf$^{\Delta iPlp1}$) results in CNS-wide demyelination[42,43]. We reasoned that additional knockout of *Myrf* from OPCs would prevent remyelination[44], so we crossed the Myrf$^{fl/fl}$ line to the pan-OL lineage CreERT line Sox10-CreERT[45] (Myrf$^{fl/fl}$ Sox10 CreERT; Myrf$^{\Delta iSox10}$) (Figure 1A). Dosing of both Myrf$^{\Delta iPlp1}$ and Myrf$^{\Delta iSox10}$ with tamoxifen at eight weeks of age (Figure 1B) results in progressive ataxia, hindlimb tremor and weight loss (Figure S1A, B). These symptoms peaked by weeks 10-12 and gradually improved in Myrf$^{\Delta iPlp1}$ mice as previously published[42,43]. In contrast, Myrf$^{\Delta iSox10}$ mice progressed to show hindlimb paresis, reduced mobility and developed seizures after 12 weeks post tamoxifen, necessitating their euthanasia (Figure S1A-B).

At the histological level, both lines showed CNS-wide demyelination by 10 weeks post tamoxifen (Figure S1, C, D). We took advantage of the optic nerve, a structure comprised of the retinal ganglion cell (RGC) axons that are nearly all myelinated[46], to compare the remyelination potential of each line (Figure 1C). By 10 weeks post tamoxifen, Myrf$^{\Delta iPlp1}$ mice had some thin myelin sheaths (g-ratio >0.80) characteristic of remyelination within the optic nerve (Figure S2A). By 20 weeks post tamoxifen, nearly 75% of the axons in the optic nerve of Myrf$^{\Delta iPlp1}$ mice were remyelinated (Figure 1D) with thin myelin (Figure S2B-D) indicative of remyelination. In contrast, Myrf$^{\Delta iSox10}$ mice had virtually no myelinated axons within the optic nerve by 10 weeks post tamoxifen consistent with an inability to remyelinate (Figure 1C, D). At 10 weeks post tamoxifen only Myrf$^{\Delta iPlp1}$ mice demonstrated increased expression of BCAS1 (Figure 1E,F), a marker of both newly-formed oligodendrocytes and their myelin[47]. This inability of Myrf$^{\Delta iSox10}$ mice to upregulate BCAS1 is indicative of a failure to generate new remyelinating oligodendrocytes.

To assess the functional consequences of remyelination failure in Myrf$^{\Delta iSox10}$ mice, we performed compound action potential (CAP) recordings at 10- and 20-weeks post tamoxifen (Figure 1G). There is increased latency in both demyelinated mouse lines and reduced CAP area (Figure 1H, I). However, remyelination present even at 10 weeks post tamoxifen in Myrf$^{\Delta iPlp1}$ mice is sufficient to improve conduction speeds relative to Myrf$^{\Delta iSox10}$ mice (Figure 1G, H). Similarly, visual-evoked potentials (VEPs) have reduced latency in Myrf$^{\Delta iPlp1}$ mice relative to Myrf$^{\Delta iSox10}$ mice at 10 weeks post tamoxifen, and normalize to non-demyelinated control levels by 20 weeks post tamoxifen (Figure 1J). Together, we have characterized two demyelinating transgenic mice lines. Myrf$^{\Delta iPlp1}$ mice feature rapid and effective remyelination which is associated with greater functional and electrophysiological recovery, and Myrf$^{\Delta iSox10}$ mice have little remyelination and worsened functional outcomes.

New oligodendrocytes are unable to fully mature in Myrf$^{\Delta iSox10}$ mice

To gain more insight into the stage of remyelination that is blocked following ablation of *Myrf* in OPCs, we performed single-nuclei RNA sequencing (snRNA-seq) of the optic nerves of Myrf$^{fl/fl}$, Myrf$^{\Delta iPlp1}$, and Myrf$^{\Delta iSox10}$ mice at 10 weeks post tamoxifen (Figure 2A). 49,806 nuclei passed quality control and were sorted into 14 distinct clusters based on well-characterized markers (Figure 2B-D). In both Myrf$^{\Delta iPlp1}$ and Myrf$^{\Delta iSox10}$ mice there is a near complete loss of the mature OL (MOL) population (Figure 2E, F), consistent with efficient recombination and loss of the developmentally-generated OLs in both lines. Myrf$^{\Delta iPlp1}$ mice had increased proportions of both the newly-formed OL (NFOL, characterized by high *Enpp6, Bcas1 and Tcf7l2*) and myelin-forming OL (MFOL, characterized by high expression of myelin genes) populations. Together, this supports active oligodendrogenesis and remyelination in these mice (Figure 2F). In contrast, Myrf$^{\Delta iSox10}$ mice formed virtually no NFOLs or MFOLs (Figure 2E, F). Accordingly, myelin protein transcripts (*Mobp, Mog*) and critical genes for OL function like *Anln* and *Trf* are not expressed in nuclei from Myrf$^{\Delta iSox10}$ mice (Figure 4G). The Myrf$^{\Delta iSox10}$ mice form committed OPCs (COPs), cells at an intermediate differentiation state characterized by the down-regulation of OPC markers *Pdgfrα* and *Cspg4* and the expression of *Bmp4* and *Fyn*. However, these cells lack the characteristic expression of *Gpr17* in Myrf$^{\Delta iSox10}$ mice and cluster separately to the COPs seen in Myrf$^{\Delta iPlp1}$ mice (COP1) (Figure 2E, Figure S4C), indicating loss of *Myrf* in OPCs disrupts their differentiation at an early stage.

To validate the snRNAseq we performed immunohistochemistry on optic nerves (Figure 2H) and found that while CC1 cells initially declined at 10 weeks post tamoxifen in Myrf$^{\Delta iPlp1}$ mice, they eventually recovered at 20 weeks back to control levels. By administrating EdU in their drinking water, we label a large number of new OLs in Myrf$^{\Delta iPlp1}$ mice indicative of considerable oligodendrogenesis (Figure S3A, C). The density of OLIG2+PDGFRα+ OPCs that incorporated EdU, as well as the total density of OLIG2+PDGFRα+ cells increased in both Myrf$^{\Delta iPlp1}$ and Myrf$^{\Delta iSox10}$ relative to Myrf$^{fl/fl}$ (Figure 2H, S3B), indicating OPC proliferation is not altered in the absence of *Myrf*. Similarly, there are few transcriptional differences detected between Myrf$^{\Delta iPlp1}$ and Myrf$^{\Delta iSox10}$ OPCs, demonstrating that *Myrf* deletion from OPCs does not result in large alterations to the OPCs prior to their differentiation (Figure S3D-F). In accordance with our snRNAseq findings, Myrf$^{\Delta iSox10}$ mice had few OLIG2+CC1+ OLs (Figure 2J) and highly reduced numbers of EdU+OLIG2+CC1+ OLs relative to Myrf$^{\Delta iPlp1}$ mice indicative of inability to robustly produce new OLs (Figure S3C). Collectively, immunohistochemical and sequencing data indicate *Myrf* knockout from OL lineage cells in Myrf$^{\Delta iSox10}$ mice results in loss of OLs with OPCs unable to differentiate beyond the COP level and generate new OLs.

One unexpected finding is the formation of a population of cells selective to the two *Myrf* conditional knockout lines, referred to as knockout OLs (KOOLs)(Figure 2F). KOOLs express OL-enriched transcription factors like *Zfp536*, *St18* but also OPC/COP transcription factors like *Sox6*, *Zeb1* and *Klf6* (Figure S4D). They have characteristically high expression of *Prex2*, *Matn2* and *Col5a3* but fail to robustly express key myelin genes and MOL markers like *Trf* and *Anln*. These cells are reminiscent of genetically fate-mapped cells we had previously found in Myrf$^{\Delta iPlp1}$ that downregulated OL markers and can persist some time before undergoing apoptosis[42]. They also express a number of markers reported to be present in disease-associated oligodendrocytes present in cuprizone[48,49] and Alzheimer's disease models[49,50] such as *Il33*, *Cdkn1a*, *Klk8* and *Serpina3n* (Figure S4E). This suggests there may be conserved transcriptional changes in damaged oligodendrocytes from several types of insults. Trajectory analysis found that this population may form via the transition of either MOLs or COP2 to KOOLs (Figure S4F). KOOLs are produced in similar proportions in both Myrf$^{\Delta iPlp1}$ and Myrf$^{\Delta iSox10}$ (Figure 2F) and their presence indicates that OL lineage cells may persist for some time following *Myrf* knockout before undergoing apoptosis.

Remyelination failure is associated with expansion of a population of microglia/macrophages characterized by lipid binding and metabolism genes

We next compared the influence of remyelination failure on the neuroinflammatory response. At the histological level, demyelination in both Myrf$^{\Delta iPlp1}$ and Myrf$^{\Delta iSox10}$ mice is associated with an increase in microglia/macrophage density (Figure 3A, B), T cell infiltration (Figure S5A, B) and astrogliosis (Figure S5C, D). The density of IBA1+ microglia/macrophages (Figure 3B), CD3+ T cell number (Figure S5B), and GFAP expression (Figure S5D) within the optic nerve do not differ between Myrf$^{\Delta iPlp1}$ and Myrf$^{\Delta iSox10}$ mice. Microglia/macrophages became activated in response to demyelination following *Myrf* knockout. The microglial/macrophage lysosomal marker CD68, which is upregulated during active phagocytosis[51], is elevated at 10 weeks post tamoxifen in both lines but declines by 20 weeks post tamoxifen in the Myrf$^{\Delta iPlp1}$ mice (Figure 3C).

To more closely assess the effects of remyelination failure on the microglia/macrophage population we subclustered this population of nuclei in the optic nerve snRNAseq dataset. We annotated five microglia clusters with three of these clusters (demyelination-induced microglia/macrophages 1-3; DIM1-3) enriched in both Myrf$^{\Delta iPlp1}$ and Myrf$^{\Delta iSox10}$ mice following demyelination (Figure 3D). DIM1-3 were distinguished from homeostatic or barrier associated macrophages (BAM) by the presence of elevated activation markers including *Ms4a7*, *Trem2*, *Axl* and *Atp6v0d2* (Figure 3E-F). The expression of these transcripts did not differ between Myrf$^{\Delta iPlp1}$ and Myrf$^{\Delta iSox10}$ mice, suggesting broadly similar activation (Figure 3G). Further, there is considerable overlap in upregulated transcripts in microglia/macrophages between Myrf$^{\Delta iPlp1}$ and Myrf$^{\Delta iSox10}$ relative to Myrf$^{fl/fl}$ mice (Figure 3H). DIM2 microglia/macrophages are characterized by elevated levels of *Igf1*, and *Spp1*, which had previously been found in a subpopulation of microglia along axon tracts[52] and may be supportive of remyelination[53] (Figure 3F). DIM3 was the only population that was increased in Myrf$^{\Delta iSox10}$ mice relative to the Myrf$^{\Delta iPlp1}$ line (Figure 3I, J). This population is characterized by a distinct set of transcripts such as *Epas1, Atp8b4, Cd38 and Aoah* (Figure 3K). Gene set enrichment analysis on DIM3 revealed the top term is phospholipid binding (Figure 3L). Accordingly, the major transcriptional differences in Myrf$^{\Delta iSox10}$ microglia/macrophages relative to Myrf$^{\Delta iPlp1}$ microglia/macrophages involved lipid binding and metabolism (Figure 3M). In summary, microglial/macrophage inflammatory responses are

broadly similar in both lines with the exception of a distinct subpopulation of microglia/macrophages increased in proportion of Myrf$^{\Delta iSox10}$ mice characterized by enriched transcription of lipid metabolism and binding genes.

Astrocytes, in contrast to microglia/macrophages, did not cluster into distinct subsets in Myrf$^{\Delta iPlp1}$ and Myrf$^{\Delta iSox10}$ mice (Figure S5E) and showed broadly similar activation following demyelination between the two lines (Figure S5E-G). One notable exception is that astrocytes in Myrf$^{\Delta iSox10}$ mice have a more prevalent upregulation of *Slc39a14* and *Cp*, transcripts encoding proteins critical for the uptake and detoxification of iron (Figure S5G). This may be an adaptive change in astrocytes to reduce oxidative stress in response to loss of OLs, the major iron-storing cells of the CNS[54].

Remyelination protects neurons from axonal damage and apoptosis

Comparing Myrf$^{\Delta iPlp1}$ mice, which feature considerable remyelination, to Myrf$^{\Delta iSox10}$ mice with remyelination failure, allows for a clear assessment of the role of remyelination in neuronal integrity. Axonal swellings with accumulated organelles are found following demyelination in both Myrf$^{\Delta iPlp1}$ and Myrf$^{\Delta iSox10}$ mice 10 weeks post tamoxifen (Figure 4A-B), indicative of impaired axonal transport, an early stage of damage[55,56]. The total number of axons did not decline by 10 weeks post tamoxifen (Figure 4C). Serum neurofilaments (NfL) has been used as a biomarker of axonal degeneration in a variety of diseases including MS[57]. Serum NfL levels are enriched at 10 weeks post tamoxifen in both Myrf$^{\Delta iPlp1}$ and Myrf$^{\Delta iSox10}$ mice (Figure 4D). These levels fell statistically in Myrf$^{\Delta iPlp1}$ mice by 20 weeks post tamoxifen, indicating that remyelination is temporally associated with a decrease in active axonal damage (Figure 4D). The staining of axons with an antibody against an epitope of neurofilament that is only exposed following proteolysis[58] further supports presence of axonal damage in Myrf$^{\Delta iSox10}$ mice (Figure 4E).

We next asked whether the cell bodies of RGCs, which project their axons through the optic nerve, are protected by remyelination. Retinal flatmounts stained with RBPMS, a pan RGC marker[59] and cleaved-caspase-3 were used to detect apoptotic RGCs (Figure 4F). Myrf$^{\Delta iSox10}$ mice have increased apoptosis in the ganglion cell layer (GCL) relative to both the remyelinating Myrf$^{\Delta iPlp1}$ mice and non-demyelinated controls (Figure 4G). While many of these cells colabeled with RBPMS+ (Figure 4H) and were selectively present in the ganglion cell layer, RBPMS is downregulated during injury[60] (Figure S6C), so it is not surprising that cleaved-caspase 3+ cells that are often faint or absent RBPMS staining (Figure 4I). Examining the total number of RGCs using RBPMS (Figure 4J), Myrf$^{\Delta iPlp1}$ mice did not have detectable loss of RGCs even at 20 weeks post tamoxifen (Figure 4K). However, we found a statistically significant decline in the number of RGCs in Myrf$^{\Delta iSox10}$ mice relative to controls by 12-weeks post tamoxifen (Figure 4L). Together, this indicates that even the partial remyelination present by 10-weeks post tamoxifen in the Myrf$^{\Delta iPlp1}$ line is protective against apoptosis and loss of RGCs.

Remyelination failure activates the DLK/JNK/c-Jun pathway in RGCs

To understand how demyelinated neurons might be damaged by a failure to remyelinate in Myrf$^{\Delta iSox10}$ mice, we performed bulk RNA-seq on the GCL of Myrf$^{fl/fl}$ and Myrf$^{\Delta iSox10}$ mice (Figure 5A). Laser dissecting the GCL greatly enriched for RGC-specific transcripts relative to whole retina (Figure 5B). Notably, the GCL of Myrf$^{\Delta iSox10}$ mice showed upregulation of *Ecel1*, *Hrk* and *Atf3*, all of which are known transcriptional targets of the DLK/JNK/c-Jun pathway in the context of traumatic axonal injury[36,37,61] (Figure 5C). *In situ* hybridization of *Ecel1* and *Hrk* confirmed that these transcripts are expressed in *Rbpms*-positive RGCs in Myrf$^{\Delta iSox10}$ mice (Figure 5D, E). DLK

and the related leucine zipper kinase (LZK) signal through MAP2Ks MKK4/7, and the MAPK JNK which directly phosphorylates the transcription factor c-Jun to drive gene expression[30,62]. To determine whether this pathway is activated in the chronically demyelinated RGCs, we examined the phosphorylation of c-Jun in retinal flatmounts (Figure 5F). Little phosphorylated c-Jun is detected in $Myrf^{fl/fl}$ mice, and only very occasional phosphorylated-c-Jun+ RGCs are present in the $Myrf^{\Delta iPlp1}$ mice. However, a large increase in the density of phosphorylated c-Jun+ cells is observed in $Myrf^{\Delta iSox10}$ mice (Figure 5G). Nearly all of these cells co-labeled with Tuj1 (Figure 5H) or RBPMS (Figure 5I), markers of RGCs. Autoimmune demyelination mediated by MOG_{35-55} (Figure S6A) also increased the phosphorylation of c-Jun in RGCs (Figure S6D), indicating the source of demyelination is not a major contributor of whether phosphorylation of c-Jun is triggered. The intensity of phosphorylated c-Jun is similar between $Myrf^{\Delta iSox10}$ mice, EAE mice and crush mice (Figure 5F, Figure S5A) is associated with apoptosis (Figure S6B, C, E). In $Myrf^{\Delta iSox10}$ mice, the onset of phosphorylation of c-Jun is coincident with decreased MBP and OLs at eight weeks post tamoxifen, indicating a tight temporal relationship between demyelination and c-Jun phosphorylation (Figure S7A-G). By 10 weeks post tamoxifen remyelination is well underway in $Myrf^{\Delta iPlp1}$ mice (Figure 1D) and is sufficient to suppress phosphorylation of c-Jun relative to $Myrf^{\Delta iSox10}$ mice (Figure 5G).

We next investigated if there is increased phosphorylation of the pathway's intermediate MAPKs, MKK4 and JNK, within the optic nerve (Figure 5J, K). The phosphorylation of both JNK and MKK4 are increased in the optic nerves of $Myrf^{\Delta iSox10}$ mice at 10 weeks post tamoxifen (Figure 5L), whereas neither kinase have detectable increases in phosphorylation in $Myrf^{\Delta iPlp1}$ mice (Figure 5M). Although total DLK levels were not altered in $Myrf^{\Delta iSox10}$ mice relative to controls, DLK's apparent molecular weight increased, consistent with activating posttranslational modifications such as phosphorylation[31] and palmitoylation[63,64] previously demonstrated after injury. In summary, $Myrf^{\Delta iSox10}$ mice have increased phosphorylation of MAPKs, c-Jun and transcription of genes associated with axonal injury and stress.

Pharmacological inhibition of DLK reduces apoptosis of demyelinated RGCs

While DLK is critical for neurodegeneration following traumatic injury[29,37,65], growth factor withdrawal[34] and in several rodent models of neurodegenerative disease[36], it has not been previously implicated in demyelinating disease. To determine whether DLK is necessary for neurodegeneration following remyelination failure, we treated $Myrf^{\Delta iSox10}$ mice with the DLK inhibitor GNE-3511[66,67] at ten weeks post tamoxifen for three consecutive days via oral gavage (Figure 6A). We found this regimen increased serum levels of GNE-3511 above 2 µM. This dose has been used to suppress the phosphorylation of c-Jun in RGCs following optic nerve crush[68] and in ALS models[36]. Retinal flatmounts were stained with RBPMS, phosphorylated c-Jun, or cleaved caspase-3 (Figure 6B, C). Treatment of $Myrf^{\Delta iSox10}$ mice with GNE-3511 returned the phosphorylation of c-Jun to baseline levels observed in $Myrf^{fl/fl}$ littermates (Figure 6D). Likewise, cleaved-caspase-3+ cells and cleaved-caspase-3+RBPMS+ levels are returned to baseline, suggesting near-complete protection from apoptosis of RGCs following acute GNE-3511 treatment (Figure 6 E and F). DLK inhibition is therefore, capable of completely suppressing both the phosphorylation of c-Jun and apoptosis within demyelinated neurons.

Genetic targeting of DLK and LZK prevents apoptosis of demyelinated RGCs

We next used a genetic strategy to determine if the neuronal MAP3Ks, DLK and LZK, leads to apoptosis of chronically demyelinated RGCs. DLK and the related MAP3K LZK have partially

redundant roles; the knockout of both MAP3Ks has been reported to synergistically promote neuroprotection *in vitro,* optic nerve crush and traumatic brain injury[65,69,70]. We developed AAVs encoding tandem sgRNAs to test if DLK is necessary for degeneration and if it works synergistically with LZK (Figure 7A). We injected AAVs with sgRNAs targeting either DLK (*Map3k12*), or both DLK and LZK intravitreally at six weeks post tamoxifen in Myrf$^{\Delta iSox10}$ and Myrf$^{fl/fl}$ mice crossed with Rosa26-Cas9 mice (Myrf$^{\Delta iSox10}$ or Myrf$^{fl/fl}$; Cas9). Control AAVs with sgRNAs targeting eGFP and LacZ were injected into the contralateral eye. All AAVs effectively labeled RGCs throughout the retina (Figure 7B). To determine whether CRISPR/Cas9 mediated knockout of DLK and LZK prevented the phosphorylation of c-Jun and apoptosis of RGCs, we stained retinal flatmounts for phosphorylated c-Jun (Figure 7C) and cleaved caspase-3+ (Figure 7D). Retinas infected with either sgDLK alone or sgDLK/sgLZK have near-complete suppression of both c-Jun phosphorylation and RGC apoptosis, with levels of each comparable to Myrf$^{fl/fl}$; Cas9 littermates without demyelination (Figure 7E-H). Together these data indicate DLK is the major MAP3K necessary for neurodegeneration following a demyelination and subsequent remyelination failure.

Discussion

Remyelination has been associated with greater protection of axons and neurons in MS[22-24], but direct experimental data showing remyelination failure causes neurodegeneration is sparse. By comparing our remyelination-capable and deficient mouse lines we find remyelination improves conduction velocity and functional recovery, while helping to maintain neuronal integrity. Remyelination suppresses the activation of the MAPKs downstream of DLK and the transcription factor c-Jun, which ultimately protects demyelinated neurons from apoptosis. We demonstrate that DLK is necessary for neuronal apoptosis using a CRISPR-mediated knockout of DLK from RGCs, and that pharmacological inhibition of DLK is sufficient to suppress c-Jun phosphorylation and neurodegeneration. We propose that neuroprotection in demyelinating disease can, in theory, be achieved by targeting retrograde signaling mediated by DLK within the neuron, or by promoting remyelination, which suppresses the same DLK-mediated signaling cascade.

The potential of genetic models of demyelination induced by *Myrf* knockout

We characterize two models of genetic demyelination induced by the knockout of *Myrf* from just OLs (Myrf$^{\Delta iPlp1}$) or OLs along with OPCs (Myrf$^{\Delta iSox10}$). Both of these models offer distinct advantages for subsequent studies. Myrf$^{\Delta iPlp1}$ mice demonstrate highly reproducible CNS-wide demyelination with clear behavioral and physiological readouts. The remyelination process begins rapidly in the optic nerves of Myrf$^{\Delta iPlp1}$ mice, even before all myelin destined to be lost has degenerated. This is in accordance with a recent live-imaging study demonstrating that remyelination can be near synchronous with demyelination replacing individual internodes as they are lost[71]. In the present study, we found the delay of conduction within the visual system correlates temporally with demyelination, whereas restoration is associated with remyelination in Myrf$^{\Delta iPlp1}$ mice. Likewise, motor function declines significantly with the onset of demyelination and partially recovers with remyelination. In contrast to Myrf$^{\Delta iPlp1}$ mice, Myrf$^{\Delta iSox10}$ mice do not effectively remyelinate and fail to recover, with the differentiation of remyelinating cells essentially blocked at the COP stage. These Myrf$^{\Delta iSox10}$ mice are the first model that cell-selectively impairs remyelination and will be a powerful genetic tool to determine how chronically demyelinated neurons may be damaged and to test neuroprotective therapeutics.

Interestingly, our snRNA-seq analysis revealed a novel population of OLs present in both lines (KOOLs) following ablation of *Myrf.* Although this KOOL population shares some markers with disease-associated OLs present in cuprizone[48,49] and Alzheimer's disease models[49,50], it also shows elevated expression of markers including *Kcnab1* and *Piezo2* and likely reflects transcriptional dysregulation following ablation of *Myrf* rather than a physiological response to demyelination (see Figure S3). Our previous studies using Myrf$^{\Delta iPlp1}$ mice with a genetic reporter demonstrated that a subset of recombined OLs persisted for a time following loss of their myelin sheaths, and it is likely these cells correspond to the KOOLs seen via snRNA-seq. Nevertheless, trajectory analysis indicates KOOLs could also form from differentiation of recombined OPCs. Genetic ablation of *Myrf* in adult OPCs has been widely used to study the role of adaptive myelination in learning[45,72-74]; some care should be taken in the interpretation of these studies given the potential for a persisting non-physiological oligodendroglial population.

Remyelination success regulates microglia/macrophage inflammation

Microglia have a crucial and well-characterized role in regulating the efficacy of remyelination[75-78]. Conversely, we demonstrate that preventing oligodendrogenesis and remyelination in Myrf$^{\Delta iSox10}$ mice can also change microglia/macrophage inflammation. Most notably, there is an increase proportion of the DIM3 population in Myrf$^{\Delta iSox10}$ mice, which is characterized by the elevated expression of a number of lipid-binding proteins and the cholesterol transporter *Apoe*. Cholesterol is the major lipid constituent of myelin and transcriptional changes in microglia are necessary for effective cholesterol uptake, lipolysis, storage and transport[79-81]. Both sterol synthesis and efflux in microglia are necessary for effective remyelination[81], presumably by acting as a source of sterols for newly generated oligodendrocytes. In Myrf$^{\Delta iSox10}$ mice, it is intriguing to consider that in the absence of new remyelinating oligodendrocytes, microglia lack a cellular source of reuptake for recycled cholesterol from damaged myelin. Increased accumulation of cholesterol within microglia and poor efflux is also associated with persistent inflammation[81]. With disease chronicity in MS, microglia become progressively more diffusely activated; it is at least conceivable that poor remyelination may contribute to persistent microglial activation[82]. Future work should determine if this distinct population of microglia/macrophages is more prone to arise during aging in which remyelination is slower and often fails.

Remyelination failure is a driver of neurodegeneration

A failure to remyelinate has been associated with greater axonal damage in neuroimaging and histopathological studies in MS[22,23]. Remyelination efficiency often wanes over time[9,12] and given the prevalence of chronically demyelinated lesions with disease chronicity, remyelination failure is likely an important contributor of axon degeneration and subsequent cell body loss. Two recent studies measuring remyelination in MS lesions using a myelin tracer with positron emission tomography (PET), support this notion. Greater perilesional tissue sparing is adjacent to lesions with more efficient remyelination, which supports a protective role of remyelination in MS[83]. Axons running through non-remyelinating lesions were more likely to be associated with brain atrophy in the cortical regions they project from[84], suggesting a dying-back loss of cortical neurons.

In spite of these correlations from human neuroimaging and pathological studies, a direct association between remyelination and neuroprotection has been difficult to establish in rodents, in part due to their efficient remyelination. Targeting the OL lineage with cell-specificity, we find that blocking remyelination leaves axons more vulnerable to damage, neurons more prone to

apoptosis and worsens functional outcomes. Conversely, accelerating remyelination by deleting the M1 muscarinic receptor from OL lineage cells increases axon preservation and functional recovery in EAE[85]. Collectively, these gain and loss of function experiments provide direct experimental evidence that remyelination rate is a critical determinant of subsequent neurodegeneration. These experiments provide an important counterpoint to recent findings that damaged or dysfunctional myelin is also a risk factor for axonal degeneration[56]. Axonal damage in EAE is more prevalent in myelinated axons relative to their demyelinated counterparts and the hypomyelinated *Mbp* mutant mouse have less axonal damage in EAE[56]. These animal studies suggest a substantial challenge for targeting myelin in MS; during the early stages of the disease on one hand dysfunctional myelin is damaging to the axon and needs to be cleared, on the other hand, prolonged demyelination is also detrimental to both the function and viability of the neuron.

DLK-mediated MAPK signaling is a retrograde cascade necessary for apoptosis of demyelinated RGCs

Axonal damage is observed prominently in demyelinating lesions during MS[25-28], but there is also neuronal apoptosis[86] and considerable loss of neurons[19,87]. Here, we find chronic demyelination of the axon increases DLK-mediated MAPK retrograde signaling and triggers neuronal apoptosis if remyelination is genetically blocked, thus linking axonal remyelination status to neuronal cell body loss. DLK-regulated MAPK signaling is a well-known activator of c-Jun mediated transcription in response to axonal injury[37,38], generally triggering apoptosis of CNS neurons[62,88,89]. c-Jun likely regulates apoptosis at least in part through modulating the expression of *Bcl2* family members like *Bbc3* and *Bcl2l2*[62,90]. Interestingly, only a small percentage (~7%) of RGCs had detectable phosphorylation of c-Jun at any given time in Myrf$^{\Delta iSox10}$ mice, despite near-complete demyelination within the optic nerve. In contrast, we found after a crush injury nearly every RGC has phosphorylated c-Jun. This could be in part due to demyelinated neurons showing intermittent phosphorylation of c-Jun, which can be rapidly induced following traumatic injury and can fall within days[91-93]. Alternatively, individual RGC subpopulations may show heterogenous vulnerability to DLK-mediated c-Jun phosphorylation and apoptosis following demyelination. Future work should examine if *Jun* is necessary for RGC apoptosis following demyelination and if particular subtypes of RGCs are preferentially vulnerable to demyelination-associated apoptosis, as has been observed following optic nerve crush[94,95].

Beyond acting as a retrograde MAPK-mediated 'death signal' to the soma, DLK may mediate degeneration locally within demyelinated axons as well. Mitochondria increase in size and content within the axon presumably to meet energy requirements to conduct following demyelination[96,97]. DLK may act on mitochondria by phosphorylating DRP1 which increases mitochondrial fission[98]. The balance between fission and fusion is crucial for maintaining energy homeostasis within the cell[99] and excessive fission triggered by DLK-mediated DRP1 phosphorylation would likely decrease energy production[100], precisely when it is needed the most following demyelination[13,14,16,101,102]. DRP1 also interacts with BAX to drive mitochondrial fragmentation and subsequent apoptosis, beginning first in the axon[100,103]. As well, DLK can degrade NMNAT2 and SCG10, labile proteins necessary for the survival of the axon[69,104]. Therefore, DLK acting locally within demyelinated axons may regulate key survival factors and potentially disrupt mitochondrial function. Future experiments should examine if DLK activation decreases these survival factors locally within the axon or increases DRP1-mediated mitochondrial fission contributing to metabolic strain within demyelinated axons.

We demonstrate that a MAPK cascade mediated by DLK is critical for neurodegeneration following demyelination. By either promoting subsequent remyelination, or by inhibiting MAPK/c-Jun signaling downstream of DLK directly blocks retrograde degeneration of the neuron. Together it suggests DLK activity is a potential therapeutic target for neuroprotection in MS. While there are a number of blood-brain barrier permeable inhibitors already produced[66,67], a recent phase one trial with a DLK inhibitor in ALS warrants caution on this approach as prolonged DLK inhibition is associated with considerable safety concerns[105]. It may be necessary to dissect and target the downstream responses induced by DLK that drive neurodegeneration in the context of remyelination failure to produce druggable therapeutic targets.

Acknowledgments

We would like to thank Peggy Assinck, Kelly Monk and Marc Freeman for critically reading and providing feedback on this manuscript. We thank Pamela Camaday for her assistance and guidance with flow cytometry. Alex Klug and Amy Carlos provided 10x microfluidics and library production support. Brian Jenkins, Hannah Bronstein and Stefanie Kaech Petrie provided guidance and support for microscopy image analysis. This work received support from the Flow Cytometry, Gene Profiling/RNA and DNA Services Shared Resource, Massively Parallel Sequencing Shared Resource, Multiscale Microscopy Core (MMC) and Advanced Light Microscopy Cores at OHSU. Paul Meraner kindly provided Cas9-expressing Neuro2a cells for sgRNA validation. This work was supported by grants from Race to Erase MS, the NINDS (R01NS120981), Collins Medical Trust (1016373), (P30 NS061800 (SAA)), and the National Multiple Sclerosis Society (RG-2001-35775). B.E. was supported by an endowment from the Warren family. G.J.D. was supported by a postdoctoral fellowship (FG-1808-32238) and a career transition award (TA-2105-37636) from the National Multiple Sclerosis Society. CC was supported by FISM - Fondazione Italiana Sclerosi Multipla – cod. 2019/BC/002 and financed or co-financed with the '5 per mille' public funding.

Author contributions

G.J.D. and B.E. designed and conceived the experiments. G.J.D., S.D.I., J.H., M.M., C.C., A.A, N.J., K.A., S.J.F., B.S. and B.E. performed experiments and acquired data. G.J.D., K.E. and J.N. curated data and provided code for analysis of the snRNAseq data. G.J.D, K.E., C.C., A.A., J.N. and B.E. analyzed data. A.M. trained and supervised G.J.D. in acquisition of CAPs from the optic nerve. J.N. trained and supervised G.J.D. and K.E. in snRNAseq analysis. T.A.W. provided expertise with MAPK reagents and biology. S.A.A., A.M., T.S., A.J.G., and B.E. provided resources or funding for the experiments. G.J.D. and B.E. wrote the manuscript with inputs from all authors. B.E. supervised the project.

Declaration of interests

B.E. is a co-founder of and has received consulting fees from Autobahn Therapeutics.

Methods

Resource Availability

Lead Contact

Further information and requests for resources and reagents should be directed to and will be fulfilled by the lead contact, Ben Emery (emeryb@ohsu.edu).

Materials Availability

All plasmids generated in this study have been deposited at Addgene (Plasmid #208834, 208835, 208836, 208837). Transgenic mouse lines are available at Jackson laboratory (Sox10-CreERT JAX #027651, Plp1-CreERT JAX 005975, Myrf$^{fl/fl}$ JAX 010607, Rosa26-Cas9 mice JAX #024858) and the Myrf$^{fl/fl}$ line on C57BL/6 background is available from the Emery lab upon reasonable request. All other reagents were from commercial sources.

Code Availability

Single-nuclei data can be viewed in our interactive browser at https://emerylab.shinyapps.io/Myrf_iCKO_OpticNerve/. All original code has been deposited at (Github: https://github.com/EmeryLab/Myrf_iCKO_OpticNerve) and is publicly available as of the date of publication. Any additional information required to reanalyze the data reported in this paper is available from the lead contact upon request.

Experimental model and subject details

Mouse lines and husbandry

All mice were housed and maintained in the Oregon Health and Science University animal facility in a pathogen-free temperature and humidity-controlled environment on a 12-hour light/dark cycle. All animal procedures were performed in accordance with, and approved by, the instructional Animal Care and Use Committee of OHSU. Myrf$^{fl/fl}$ mice were generated in the Barres laboratory[40] (B6;129-*Myrf*^{tm1Barr}/J) and crossed to either Plp1-CreERT[106] (B6.Cg-Tg[Plp1-cre/ERT]3Pop/J) to delete *Myrf* from OLs or Sox10-CreERT mice[45] (CBA;B6-Tg[Sox10-icre/ERT2]388Wdr/J) to delete *Myrf* from both OLs and OPCs. To allow for CRISRP/Cas9 mediated disruption of genes, Myrf$^{\Delta iSox10}$ mice were crossed to constitutively-expressing Cas9 mice under the Rosa26 promoter[107] (Gt[ROSA]26Sortm1.1[CAG-cas9*,-EGFP]Fezh/J, JAX :024858) to produce Myrf$^{\Delta iSox10}$ Cas9 and Myrf$^{fl/fl}$ Cas9 mice. In all cases CreERT negative littermates served as non-demyelinated controls. Genotypes were determined by PCR analysis of ear clips, using established primers for each line, and revalidated at experimental endpoint. All experiments were conducted in both sexes of eight week-old mice. Every week following tamoxifen administration mice were weighed and health assessments performed. When mice reached a motor score of three, indicated by ataxia and significant hindlimb weakness, they received soft food on the bottom of their cage to encourage hydration. After 12 weeks post-tamoxifen, Myrf$^{\Delta iSox10}$ mice developed seizures and were not taken out past this point.

Cas9-expressing Neuro2a cell culture

Mouse Neuro2a cells (CCL-131, ATCC) expressing Cas9 (cells were transduced with Cas9 in the pQXCIH plasmid) were grown in Dulbeco's modified Eagle medium (11960-044, Gibco) (DMEM) with 10% FBS supplemented with glutamine (25030-081, Gibco), Penicillin-Streptomycin (100 U/mL penicillin, 100 mg/mL streptomycin;15140-122, Gibco); and Sodium Pyruvate (11360-070, Gibco). Neuro2a cells were incubated at 37 °C and 5% CO_2 and were passaged every three days. To transfect Neuro2a cells with sgRNA expressing plasmids, we used Lipofectamine 2000 (52758, Invitrogen) and the cells were collected 24 hours later and

DNA extracted using DNeasy Blood and Tissue Kit as per the manufacturer's instructions (69504, Qiagen).

Method Details

Tamoxifen administration

Tamoxifen (T5648, Sigma) was dissolved in corn oil (C8267, Sigma) at 20 mg/mL using heat (37°C) and agitation. Mice received intraperitoneal injections at 100mg/kg for five consecutive days at eight weeks of age. Tamoxifen was prepared fresh prior to administration for each cohort of mice.

EdU administration

To examine proliferation of OPCs and differentiation of new oligodendrocytes, we administered 5-ethynyl-2′-deoxyuridine (EdU) in the drinking water starting the week after tamoxifen injections until 10 weeks post-tamoxifen. EdU (NE08701, Carbosynth) was dissolved in water along with 0.2mg/mL of dextrose (D16-500, Fisher) to encourage consumption. This dose was previously determined to be non-toxic and able to label nearly all proliferative OPCs if administered for at least seven weeks in water[108]. EdU water was changed every two to three days over the course of administration.

GNE-3511 administration

GNE-3511 (5331680001, Millipore-Sigma) was emulsified into 0.5% methylcellulose (M7140, Sigma) with 0.2% Tween 80, and vortexed prior to oral gavage[36]. At 10 weeks post tamoxifen administration, $Myrf^{\Delta iSox10}$ mice and $Myrf^{fl/fl}$ controls received two daily gavages with either GNE-3511 at 75mg/kg or vehicle only. Gavages were at least eight hours apart for three consecutive days, for a total of six gavages.

EAE induction

Experimental autoimmune encephalomyelitis (EAE) was induced in eight week-old female C57BL/6 via immunization with myelin oligodendrocyte glycoprotein $(MOG)_{35-55}$ (PolyPeptide Laboratories). 200 µg MOG_{35-55} was dissolved in complete Freund's adjuvant containing 400 µg of *Mycobacterium tuberculosis* (231141, Difco) and injected subcutaneously in 0.2mL volume per mouse. Pertussis toxin (181, List Biological labs Inc) was administered via intraperitoneal injection after the MOG_{35-55} injection and two days later at 75ng and 200ng per mouse doses, respectively.

Intravitreal injections

Intravitreal injections of viruses containing tandem sgRNAs were used to induce Cas9-mediated disruption of *Map3K12* and *Map3K13*. $Myrf^{\Delta iSox10}$ Cas9 mice were anaesthetized with ketamine/xylazine (ketamine 100 mg/kg and xylazine 12 mg/kg). Proparacaine (NDC 13985-611-15, Akorn Inc) and tropicamide (NDC 17478-102-12, Akorn Inc) eye drops were applied to provide local analgesia and better visualization of the injection, respectively. One eye received AAV expressing small guide RNAs against LacZ and GFP under U6 promoters (AAV2-U6-sgLacZ-U6-sgGFP-hSyn1-mCherry) with the opposite eye receiving sgRNAs against *Map3K12* (DLK), or both *Map3K13* (LZK) and *Map3K12* (DLK). The concentration of viruses was adjusted to 2.8 $x10^{12}$ genome copies per mL immediately prior to injection in sterile 1x PBS. Under stereo microscopic control, the ora serata was incised with a 30□gauge needle without touching the

lens. AAV vectors (1 µL/injection) were delivered into the vitreous through the incision using a 5 µL Hamilton microinjection syringe with a blunt 30 gauge needle. After injection, paralube ophthalmic ointment (NDC 17033-211-38, Dechra) was applied and mice were placed on a heating pad until they awoke.

Optic Nerve Crush

Mice were prepared for surgery with the same ketamine/xylazine induced anesthesia as above. The right eye of each animal received an incision of the superior conjunctiva exposing the optic nerve, with care to avoid lesioning the orbital sinus. The nerve was crushed approximately 0.5mm from the optic disk for 10 seconds using fine forceps (Dumont, #5). Following surgery paralube ophthalmic ointment was applied and the mouse was placed on a heating pad until it was awake.

Compound action potentials recordings and analysis

Mice were deeply anaesthetized with ketamine and xylazine as above and an incision was made to expose the dorsal skull. The optic nerves were cut just behind the optic disk. The dorsal skull was then removed and olfactory bulbs were cut with fine surgical scissors, and the brain was gently lifted to expose the optic chiasm. The optic chiasm was then cut and optic nerves were carefully removed and placed in oxygenated artificial cerebrospinal fluid (aCSF) (124mM NaCl, 1mM NaH_2PO_4, 2.5 mM KCl, 26 mM $NaHCO_3$, 10mM glucose, 1 mM Na Ascorbate, 1mM $MgCl_2$, 2mM $CaCl_2$). Glass suction electrodes were prepared by heating the ends of glass capillaries over a flame until the tip was slightly constricted to match the nerve diameter, then bending the electrode ~30 degrees a few millimeters away to form a bent electrode to facilitate nerve holding. A silver wire was inserted into both recording and stimulating electrodes, and a reference wire was coiled around the electrodes to form a connection with the bath. Both electrodes were filled with aCSF. The optic nerve was transferred to a recording chamber with continuously perfused with aCSF and held in place with wettened filter paper. Using gentle suction, the chiasmal side of the nerve was drawn into the recording electrode and the retinal side into the stimulating electrode. The nerve was then allowed to acclimate for 30 minutes to allow the tissue to form a seal with the constricted tip of the glass electrodes before recording began. The stimulating electrode was connected to a constant current isolated stimulator unit (Digitimer DS3) and nerves were stimulated at increasing amplitudes from 0.2mA to 2mA at 0.2 Hz for 100 µs until supramaximal threshold was found. Nerves were stimulated at 125% supramaximal threshold for recordings used in quantifications[109]. Signals from the recording electrode were digitized via a Digidata 1440B, amplified using an Axon Instruments Multiclamp 700B amplifier and recorded using Clampex 10.7 software (Molecular Devices). CAP curves were subtracted from recordings following administration of TTX (1µm, HB1035 HelloBio). Data was then analyzed using the Clampfit10 software and to find both the latency to the highest peak and CAP area. CAP area is proportional to the number of stimulated axons[110], and was measured as the area of the positive voltage deflection following stimulus. Each mouse was considered a biological replicate, and one nerve was measured from each mouse.

Visual evoked potential recordings

Low ambient light (13-18 Lux) were ensured in the room where VEPs were recorded. Mice were anesthetized via intraperitoneal injection using both xylazine (12.5 mg/kg) and ketamine (87.5 mg/kg) diluted in PBS. Pupils were dilated with Tropicamide eye drops administered to each eye

precisely six minutes after ketamine/xylazine administration. Mice were then placed in a sealed cardboard box (12x12x16 cm) for five minutes for dark adaptation. 1cm steel needle electrodes (Natus Neurology) for the flash VEP were placed medially under the skin between the two eyes along the sagittal suture, with the needle inserted 8mm to optimize proximity to the visual cortex. A needle electrode inserted subcutaneously just above the tip of the nose served as reference electrode and an additional electrode inserted into the tail served as the ground electrode. A dome was next lowered to reduce ambient light and VEP stimulation and recording began precisely 13 minutes after administration of anesthesia. Flash based binocular visual electrophysiology was measured using an Espion Diagnosys system (Diagnosys LLC). Examinations consisted of 3 runs, with the following characteristics: pulse intensity 3 cd.s/m2, frequency 1 Hz, on-time 4 ms, pulse color: white-6500K, 100 sweeps per acquisition as per[111]. The standard VEP waveform with these parameters was characterized by a prominent negative deflection after approximately 70 ms which we identified as N1. N1 was defined as the first negative deflection after 50 ms. The two most representative/reproducible waves wave were used for analysis. The exam was performed by an operator blinded to mouse genotype.

Tissue Processing

Mice were deeply anaesthetized with ketamine (400 mg/kg) and xylazine (60 mg/kg) then transcardially perfused with 10mL of PBS and 40mL of freshly hydrolyzed 4% paraformaldehyde (19210, Electron Microscopy Sciences). Tissues were gently dissected and placed in 4% paraformaldehyde for post fixation. For optic nerves used for electron microscopy, nerves were post fixed in 2% paraformaldehyde (15710, Electron Microscopy Sciences) with 2% glutaraldehyde (16310, Electron Microscopy Sciences) instead of 4% paraformaldehyde. For immunohistochemistry, optic nerves were post fixed for two hours, brains overnight, retinae for one hour and spinal cords for four hours. Optic nerves, brains, and spinal cords were then cryoprotected in 30% sucrose for at least 48 hours. Tissues were embedded in OCT and frozen on dry ice and stored at -80°C until sectioning on a cryostat (Leica CM3050-S). Brain sections were mounted at 10 µm thickness on Superfrost Plus slides (1255015, Fisher Scientific) between 1.4mm to -0.6mm relative to bregma. Optic nerve sections were made between 2-4mm retinal to the optic chiasm mounted at 10 µm thickness. All sections were stored at -80°C until immunohistochemistry was performed. Eyes were washed with 1x PBS following post-fixation and the retinae were dissected and post-fixed in 4% paraformaldehyde for 30 minutes and washed three times in 1x PBS. Retinae for *in situ* hybridization were flash frozen on dry ice following intracardiac perfusion with 1x PBS.

Immunohistochemistry

Slides were thawed from the -80°C until dry and then rehydrated in 1x PBS. For MBP staining, tissue delipidization was performed by immersing slides in ascending and descending ethanol solutions before being washed 3x in 1x PBS. Slides were blocked for 30 minutes at room temperature with 10% fetal calf serum (SH30910.03, Cytiva) with 0.2% Triton-X100 (10789704001, Sigma). Primary antibodies were applied overnight in 1x PBS with 0.2% Triton-X100 in a sealed container at room temperature. Primary antibodies included mouse anti-BCAS1 (1:200; sc-136342, Santa Cruz), chicken anti-MBP (1:200; MBP, Aves), mouse anti-CC1 (1:500; OP80, Millipore), rabbit anti-OLIG2 (1:500; AB9610, Millipore), goat anti mouse-PDGFRα (1:200 AF1062, R&D Systems), mouse anti-degenerating neurofilament light chain (1:500; MCA-6H63, Encor Biotechnology), rat anti-CD68 (1:500; MCA1957GA, Biorad), rabbit anti-Iba1 (1:1000; 019-19741, Wako), rabbit anti-GFAP (1:1000, Z0334, Dako), rabbit anti-

cleaved caspase-3 (1:200; 559565, BD Pharminogen) and rabbit anti-cleaved caspase-3 (1:200; AF835, R and D Systems). Following incubation with primary antibodies, slides were washed 3x in 1x PBS before appropriate Alexa Fluor 488, 555 or 647 secondary antibodies (Invitrogen) were applied for two hours at room temperature. Slides were then again washed 3x with 1x PBS before coverslipping with Fluoromount G (0100-01, Southern Biotech) for analysis.

For EdU labeling, slides with optic nerve sections were incubated at room temperature for 30 minutes protected from light in freshly-prepared Alexa-647 EdU Cell Proliferation Assay (C10340, Thermo Fisher Scientific) cocktail after immunohistochemistry. Slides were washed 3x in 1x PBS and coverslipped in Fluoromount-G (01001-01, Southern Biotech).

Retinal flatmounts were blocked in 10% fetal calf serum with 0.2% Triton-X100 for 1 hour with agitation. Retinae were then incubated with primary antibodies at 4°C with agitation in 1x PBS 0.2% Triton-X100. Primary antibodies included guinea pig anti-RBPMS (1:500; 1832, Phosphosolutions), rabbit anti-RBPMS (1:500 ABN1362, Millipore), mouse anti-β3 Tubulin (1:1000; T8660, Sigma), rabbit anti-phosphorylated c-Jun (1:500, 9261 Cell Signaling) and rabbit anti-cleaved caspase-3. Appropriate secondary antibodies were applied overnight with agitation at 4°C. To prepare for mounting on slides, each retina was cut with 4-5 incisions along the radial axes from the edge to about 2/3rds the distance to the optic disk then mounted on slides. Prolong Glass Antifade Mountant (P36980, Thermo Fisher Scientific) was applied prior to coverslipping.

In situ hybridization

RNAscope *in situ* hybridization was used to detect *Rbpms* (527231, ACDBio) in combination with *Ecel1* (1137301-C2, ACDBio) or *Hrk* (475331-C3, ACDBio). The assay was performed according to the manufacturer's instructions (RNAscope Multiplex Fluorescent V2 Assay, ACDBio). Briefly, 20 µm thick sections were mounted on Superfrost slides (1255015, Fisher Scientific) and stored at -80°C until *in situ* hybridization was performed. Slides were dehydrated in 50%, 70%, and 100% ethanol for five minutes before being placed into boiling target retrieval buffer for five minutes to unmask the target RNA. Slides were treated with H_2O_2 for 10 minutes at room temperature then Protease III was applied for 30 minutes at 40°C. Probes were hybridized for two hours at 40°C. Either *Ecel 1* or *Hrk* was assigned to channel 2 or 3 and diluted 1:50 in *Rbpms* probes assigned to channel 1. To test RNA integrity within the tissue, probes against housekeeping genes *Polr2a*, *Ppib* and *Ubc* (320881, ACDBio) were applied to slides cut in parallel along with 3-Plex negative control probes on an additional slide (320871, ACDBio). Signal amplification was performed according to the instructions of the kit. Signal detection utilized Opal520 (OP-001001, Akoya) and Opal 690 (OP-00106, Akoya), which were diluted 1:1000 in TSA buffer (322809, ACDBio). Nuclei were detected by DAPI stain applied for five minutes prior to coverslipping with Prolong Gold (P36934, Thermo Fisher Scientific).

Electron microscopy tissue processing and analysis

Following postfixation, optic nerves were stored in a buffer of 1.5% paraformaldehyde, 1.5% glutaraldehyde, 50mM sucrose, 22.5mM $CaCl_2 2H_2O$ in 0.1M cacodylate buffer for at least seven days before embedding[112]. Optic nerves were trimmed to 2mm from the optic chiasm prior to plastic embedding. Optic nerves were post-fixed in 2% osmium tetroxide (19190, Electron Microscopy Sciences) with 1.5% potassium ferrocyanide (25154-20, Electron Microscopy Sciences) using a Biowave Pro+ microwave (Ted Pella). Contrast was enhanced by *en bloc* staining with 0.5% uranyl acetate (22400, Electron Microscopy Sciences), before dehydration in

ethanol and embedding in Embed 812 (14120, Electron Microscopy Sciences). 0.5 µm sections were cut on an ultramicrotome and stained with 0.5% Toluidine Blue (22050, Electron Microscopy Sciences) with 0.5% sodium borate (21130, Electron Microscopy Sciences) to visualize the optic nerve for area measurements. 60nm sections were mounted on copper grids (T400-Cu, Electron Microscopy Sciences) then cut and counter stained with 5% Uranyl Acetate for twenty minutes followed by Reynold's Lead Citrate (80 mM $Pb(NO_3)_2$ 17900-25, Electron Microscopy Sciences and 120mM Sodium Citrate, 21140, Electron Microscopy Sciences) for six minutes. Grids were imaged at 4800x on a FEI Tecnai T12 transmission electron microscope with a 16 Mpx camera (Advanced Microscopy Techniques Corp). The density of myelinated axons was measured within each individual mesh grid in 5µm x 5µm regions for a total of 16-22 images per optic nerve. We then multiplied the average density of axons within the optic nerve by the area measured on the adjacent Toluidine Blue section to get the total number of axons. For g-ratio analysis, every fourth image was analyzed (5-6 per animal) and the axon and myelin were manually traced with the spline contour tool using the Zen 3.0 software (Zeiss) to determine the axon diameter relative to the axon diameter with myelin. Demyelinated axons were not included in the analysis and analysis was conducted blinded to genotype.

Serum neurofilament light chain (NfL) detection

After deep anesthesia with ketamine and xylazine as above, 0.5mL blood was acquired from mice immediately prior to perfusion via intracardiac puncture. Blood was allowed to clot for 1 hour before spinning at 1,500g for 10 minutes. The serum was removed and snap frozen on dry ice and stored at -80°C. NfL concentration was measured on the Simoa platform using the NF-light advantage kit V2 (Quanterix). To account for the high concentrations found in demyelinating mice that might go beyond the highest point of the calibrator, serum was bench-diluted to 1:4 or 1:8 (depending on available sample volume). On the Simoa, another 1:4 online dilution followed as part of the standard assay procedure, and final concentration was corrected for the applied dilution factor.

Immunofluorescence image analysis

Immunostained sections were captured with a Zeiss ApoTome2 at 20x using 0.8NA lens. Optic nerve cross sections were imaged in their entirety with at least four sections 200 µm apart analyzed per mouse, per analysis. For cellular counts of OL lineage cells, the optic nerve was manually outlined using the spline contour tool in Zen 3.0 (Zeiss) and OLIG2-positive nuclei were counted first. Each OLIG2-positive cell was examined to see if it expresses CC1, PDGFRα or EdU. For microglial and T-cell counts, only Iba1-positive or CD3-positive cells with DAPI nuclear staining were considered to be positive. For analysis of BCAS1, MBP and CD68 images were exported as Tiffs with the same dynamic range boundaries between animals and manually thresholded by an observer blinded to genotype and timepoint in Fiji ImageJ 1.53 (NIH) to determine the area occupied relative to the size of the optic nerve.

Retinae were imaged in their entirety for analysis at 20x with 0.8NA lens using a Zeiss ApoTome2. To quantify RBPMS or phosphorylated c-Jun, cells were manually counted in the GCL within a 200 µm x 200 µm box placed at 500 µm, 1000 µm, 1500 µm and 2000 µm from the optic disk in each quadrant for a total of 16 regions. Cleaved caspase-3-positive cells were counted over the extent of the retina. The retina was manually outlined using the spline contour tool (Zen 3.0, Zeiss) to determine the area for density measurements. All analyses were conducted blind to genotype or treatment.

Western blot

Mice were deeply anesthetized as above and perfused with 1x PBS before the optic nerve was removed and flash frozen on dry ice and stored at -80°C until protein was extracted. Thawed optic nerves were dounce homogenized in RIPA buffer along with complete protease inhibitors (11836153001, Roche). Following homogenization, samples were spun at 13,000g for 15 minutes and the protein lysate was removed and frozen. Lysates from four nerves (two mice) were combined and protein was run on Bis-Tris-gel (NP0335BOX, Invitrogen). To transfer to a PVDF membrane (IPVH00010, Thermo Scientific), the gel blotting sandwich cassette (A25977, Thermo Fisher Scientific) was placed in transfer buffer (NP0006-01, Thermo Scientific) under 20V for one hour. Following a successful transfer, blots were rinsed in 1x TBS with 0.1% Tween-20 (TBST) before blocking in 1x TBST with 5% milk powder for one hour. Blots were probed with antibodies against DLK (GTX124127, Genetex), pMKK4 (9156, Cell Signaling), MKK4 (9152, Cell Signaling), pJNK (9251, Cell Signaling), JNK (9525, Cell Signaling), MOG (supernatant from clone 8-18C5, kind gift of R. Reynolds, Imperial College, London, UK), MBP (MAB386, Millipore) with 2% BSA (BP9706-100, Fisher Scientific) overnight. After overnight incubation, blots were washed in 1x TBST and incubated with appropriate HRP-conjugated secondary (Goat anti-rat 7077, Cell Signaling, Goat anti-mouse 7076, Cell Signaling, Goat anti-rabbit 7074, Cell Signaling) for two hours with 2% milk powder in TBST. Immunoreactivity was visualized using chemiluminescence (34080, Thermo Fisher Scientific) and imaged on a Syngene GBox iChemiXT. Blots were subsequently re-probed with β-actin-HRP as a loading control (A3854, Sigma). Densitometric analysis was performed in ImageJ 1.53 by quantifying the intensity of bands relative to loading control and then normalized relative to the mean of the $Myrf^{fl/fl}$ control group.

Laser capture microscopy

Eyes were dissected and snap frozen in OCT, then sectioned on a cryostat at 20 µm thickness and mounted onto Poly-L-Lysine (P1524, Sigma) coated membrane slides (414190-9041-000, Zeiss). Sections were fixed in 70% ethanol for two minutes before staining in Harris Modified Hematoxylin (HHS32, Sigma) with 0.2% glacial acetic acid for 30s. Sections were then immersed in 70% ethanol twice, before being immersed in 100% ethanol twice for 30s each and stored at -80°C in a sealed container until LCM was performed. A Zeiss Palm Microbeam microscope was used to conduct LCM with cut segments extracted onto the lid of adhesive cap tubes (415190-9181-000, Zeiss). The GCL was identified and sectioned—at least 20 sections per animal. For sampling of the whole retina, laser incisions were made through each retinal layer. Samples were treated with RLT lysis buffer and RNA isolated using the MicroRNAeasy kit (74004, Qiagen) as per the manufacturer's instructions and frozen -80°C until sequencing.

Bulk RNAseq

Following RNA isolation, RNA quantity and quality were evaluated on an Agilient 2100 Bioanalyzer using the Eukaryote Total RNA Pico. cDNA libraries were produced by loading 15ng of RNA for use with the Illumina Stranded Total RNA Prep, Ligation with Ribo-Zero Plus kit and sequenced with a NovaSeq 6000 at 50 million reads per sample. Raw reads were sorted based on barcodes and FASTQC files were produced. Reads were aligned to *Mus musculus* (GRCm38/Mm10) and expression counts were performed using STAR. DeSeq2 was run using Basepair software to determine differentially expressed genes between whole retina and the

GCL or between the GCL of Myrf$^{\Delta iSox10}$ and Myrf$^{fl/fl}$ mice. A total of six Myrf$^{fl/fl}$ and six Myrf$^{\Delta iSox10}$ were compared for statistical analyses.

Nuclei isolation and snRNAseq

Blood was removed from deeply anesthetized mice via intracardiac perfusion with 10mL of 1x PBS at 4-7 PM to reduce circadian fluctuations. Optic nerves were dissected out and immediately snap-frozen on dry ice. Frozen tissue was stored at -80°C for up to six months until subsequent processing. The nuclei isolation buffer (NIB, 146 mM NaCl, 5 mM Tris-HCl, 1 mM $CaCl_2$, 21 mM $MgCl_2$, 0.03% Tween-20, 0.01% BSA, 1 µg/mL actinomycin D, pH 7.5) was prepared with one tablet of protein inhibitor cocktail (cOMPLETE Mini lacking EDTA, 11873580001, Roche) along with 15uL of RNAsin (N2615, Promega) per 10 mL NIB. When optic nerves were removed from the freezer, they were immediately placed in cooled 2mL NIB solution in a 7mL Dounce grinder and ground 20 times with a loose pestle. Then, the homogenate was passed through a 200 µm strainer (43-50200-03, Pluriselect). The homogenate was ground 10 additional times with a tight pestle, then 2 mL NIB was added and the homogenate was passed through a 40 µm strainer (43-50040-03, Pluriselect). The homogenate was ground five times with a tight pestle (B), then passed through a 20 µm filter (43-50020-03, Pluriselect). The sample was then centrifuged at 500g for five minutes at 4°C three times with the supernatant discarded and new NIB added each time. Following the last centrifugation step, the pellet was resuspended in 0.5 mL NIB with 5 µL SuperaseIN (AM2696, Thermo Fisher Scientific) along with 1% BSA and mixed 1:200 with RedDot (40060, Biotium). The samples were then isolated from debris by fluorescence-activated nuclei sorting (FANS). Two main gates were used: a 561+683 emission for the RedDot stain and a low trigger pulse width as singlet discriminator. 100,000 nuclei were aimed to be sorted. Following sorting, samples were centrifuged at 300g for one minute at 4°C, held on ice for one minute then spun for one minute at 300g at 4°C. The top supernatant was carefully removed and the nuclei were then prepared for snRNAseq using a Chromium Next GEM Single Cell 3′ Reagent Kit v3.1 (10x Genomics). Single nuclei were partitioned in droplets with single gel beads, which contained primers with cell-tagging indexes. Single nucleus suspensions were targeted to 10,000 nuclei per sample with 500 million reads per sample. The resulting cDNA was used as a template for library preparation. Samples were sequenced using a NovaSeq 6000 and FASTQ files were prepared using bcl2fastq (Illumina) and then aligned to the mouse GRCm38/mm10 reference genome using Cellranger (v7.0.0, 10x Genomics). Reads were mapped to both exonic and intronic regions.

snRNA-seq analyses

Data was analyzed using R (v4.2.1) and the Seurat package (v4.3.0)[113]. First, quality control of each sample was performed. Ambient RNA was removed using SoupX[114] (v1.6.2). To remove doublets and debris, nuclei were filtered based on 1,000 < nFeature_RNA < 4,000 as well as 1,250 < nCount_RNA < 10,000. Mitochondrial genes were removed by manually excluding all features starting with "mt-". One sample (a Myrf$^{fl/fl}$ sample) failed quality control and was not included in further analysis. Following quality control, the seven samples were normalized with '*SCTransform*[115]' (v0.3.5) and integrated using '*FindIntegrationAnchors*' function in Seurat. The integrated dataset was visualized by UMAP plotting techniques. Nuclei were first clustered using 35 principal component dimensions. Differentially expressed genes (DEGs) were identified using Seurat's '*FindMarkers*' with the following analysis criteria: Log2 fold change > 0.322, the

minimum percentage of nuclei expressing the gene = 0.25, and adjusted p-value (calculated with the Wilcox significance test) < 0.05. Top genes were used to identify each cluster.

Several samples had neuronal nuclear contamination from the dissection indicated by nuclei with high *Rbfox3, Syt7*, and *Snap25* and these clusters were manually excluded. After the neuronal contamination was removed, we re-clustered using 33 principal component dimensions to account for the removal of a highly diverse neuronal population that may have affected the original UMAP clustering. We re-ran the DEG analysis for the final UMAP clustering using the analysis criteria stated above and annotated the clusters with their identities. Next, we compared the DEGs between the control mice derived from different lines ($Myrf^{fl/fl}$; Plp1-CreERT-negative and $Myrf^{fl/fl}$; Sox10CreERT-negative) using the analysis criteria stated. Because both control lines had less than 10 DEGs in total, for the ease of analysis between genotypes, we combined the three control samples (hereby referred to as $Myrf^{fl/fl}$). After combining the controls, DEGs between $Myrf^{fl/fl}$ and $Myrf^{\Delta iPlp1}$ or $Myrf^{\Delta iSox10}$ were identified with the analysis criteria. Likewise, DEGs between the two knock-out lines ($Myrf^{\Delta iPlp1}$ or $Myrf^{\Delta iSox10}$) were identified using the analysis criteria above.

For microglia re-clustering, we subdivided these cells and reclustered using eight principal component dimensions based off the elbowplot. DEGs for microglia subclusters were identified with the same analysis criteria as above. DIM3 population DEGs were calculated with the following analysis criteria: log2 fold change > 0.01 and visualized with a volcano plot (ggplot2 3.42). Gene set enrichment analysis (GSEA) for molecular function pathways was performed on the DIM3 cluster differentially expressed genes (p adjusted < 0.05) using ClusterProfiler[116] (v4.6.2). Trajectory pathway analysis in psuedotime was performed on the oligodendrocyte lineage using Monocle3 (v1.3.1).

Production of viral constructs

SgRNAs were designed using CRISPROn[117] and compared to sgRNAs previously used in (Summers et al.)[104]. Five sgRNAs for *Map3K12* and *Map3K13* were tested in total for indel formation in cultured Neuro2a cells expressing Cas9. Px333 (Addgene # 64073) was modified by restriction enzymes to insert oligonucleotides with the MluI site and ApaI site at the XhoI and KpnI sites, respectively. This allows the removal of tandem U6 promoters with sgRNAs and insertion into AAV-U6-sgRNA-hSyn-mCherry (Addgene #87916) in place of the single U6-sgRNA when digested with MluI and ApaI. SgRNAs were tested in the modified px333 plasmid and validated by TIDEs (tracking of indels by decomposition)[118]. The two best sgRNAs were chosen based on the degree of decomposition after the PAM site. While all sgRNAs tested demonstrated decomposition after the PAM site, the sgRNAs which were used in the study to target *Map3K12* at exons 4 and 9 had the highest decomposition and have the following sequences AGGGTGTTCGGGTTTCATGG and TGTAGAGAGCACATCAGCGG. The guides utilized against *Map3K13* had the sequences TCTGGGGAACAGCAACACTG and GGTCACGGTGTATAATCTTG[104] targeting exons 3 and 5 of *Map3K13*, respectively. SgRNAs against LacZ and GFP for the control AAV were taken from previously validated sgRNAs[119,120]. Large-scale packaging into AAV2 of viral vectors for intravitreal injection was completed by Vector Biolabs (AAVs with sgRNAs against *Map3K12*, *Map3K13* or *Map3K12*/*Map3K13*) or Vector Biosystems (sgLacZ/sgGFP).

Quantification and Statistical Analysis

Statistical analyses were conducted with Prism 10 (Graphpad) and all data is presented as mean ± standard error. In all cases the figure legend indicates the statistical test used along with associated p-values. Sample sizes are indicated by the number of dots in the figures or are otherwise explicitly stated. For all statistical analyses *n* represents a single animal, except for the optic nerve snRNAseq and western blots, where two animals worth of nerves were combined per sample (n). Degree of significance was indicated in figures by * = $p < 0.05$, ** $p < 0.01$, *** $p< 0.001$ or **** $p < 0.0001$ unless stated otherwise. Animals were assigned to group based on genotype or to treatment by random selection. The number of mice used in experiments was based on previous publications with similar methodology.

References

1. Zawadzka, M., Rivers, L.E., Fancy, S.P., Zhao, C., Tripathi, R., Jamen, F., Young, K., Goncharevich, A., Pohl, H., Rizzi, M., et al. (2010). CNS-resident glial progenitor/stem cells produce Schwann cells as well as oligodendrocytes during repair of CNS demyelination. Cell Stem Cell *6*, 578-590. 10.1016/j.stem.2010.04.002.
2. Gensert, J.M., and Goldman, J.E. (1997). Endogenous progenitors remyelinate demyelinated axons in the adult CNS. Neuron *19*, 197-203. 10.1016/s0896-6273(00)80359-1.
3. Watanabe, M., Toyama, Y., and Nishiyama, A. (2002). Differentiation of proliferated NG2-positive glial progenitor cells in a remyelinating lesion. J Neurosci Res *69*, 826-836. 10.1002/jnr.10338.
4. Keirstead, H.S., and Blakemore, W.F. (1997). Identification of post-mitotic oligodendrocytes incapable of remyelination within the demyelinated adult spinal cord. J Neuropathol Exp Neurol *56*, 1191-1201. 10.1097/00005072-199711000-00003.
5. Jeffries, M.A., Urbanek, K., Torres, L., Wendell, S.G., Rubio, M.E., and Fyffe-Maricich, S.L. (2016). ERK1/2 Activation in Preexisting Oligodendrocytes of Adult Mice Drives New Myelin Synthesis and Enhanced CNS Function. J Neurosci *36*, 9186-9200. 10.1523/JNEUROSCI.1444-16.2016.
6. Duncan, I.D., Radcliff, A.B., Heidari, M., Kidd, G., August, B.K., and Wierenga, L.A. (2018). The adult oligodendrocyte can participate in remyelination. Proc Natl Acad Sci U S A *115*, E11807-E11816. 10.1073/pnas.1808064115.
7. Neely, S.A., Williamson, J.M., Klingseisen, A., Zoupi, L., Early, J.J., Williams, A., and Lyons, D.A. (2022). New oligodendrocytes exhibit more abundant and accurate myelin regeneration than those that survive demyelination. Nat Neurosci *25*, 415-420. 10.1038/s41593-021-01009-x.
8. Mezydlo, A., Treiber, N., Ullrich Gavilanes, E.M., Eichenseer, K., Ancau, M., Wens, A., Ares Carral, C., Schifferer, M., Snaidero, N., Misgeld, T., and Kerschensteiner, M. (2023). Remyelination by surviving oligodendrocytes is inefficient in the inflamed mammalian cortex. Neuron *111*, 1748-1759 e1748. 10.1016/j.neuron.2023.03.031.
9. Goldschmidt, T., Antel, J., Konig, F.B., Bruck, W., and Kuhlmann, T. (2009). Remyelination capacity of the MS brain decreases with disease chronicity. Neurology *72*, 1914-1921. 10.1212/WNL.0b013e3181a8260a.
10. Patani, R., Balaratnam, M., Vora, A., and Reynolds, R. (2007). Remyelination can be extensive in multiple sclerosis despite a long disease course. Neuropathol Appl Neurobiol *33*, 277-287. 10.1111/j.1365-2990.2007.00805.x.

11. Patrikios, P., Stadelmann, C., Kutzelnigg, A., Rauschka, H., Schmidbauer, M., Laursen, H., Sorensen, P.S., Bruck, W., Lucchinetti, C., and Lassmann, H. (2006). Remyelination is extensive in a subset of multiple sclerosis patients. Brain *129*, 3165-3172. 10.1093/brain/awl217.
12. Frischer, J.M., Weigand, S.D., Guo, Y., Kale, N., Parisi, J.E., Pirko, I., Mandrekar, J., Bramow, S., Metz, I., Bruck, W., et al. (2015). Clinical and pathological insights into the dynamic nature of the white matter multiple sclerosis plaque. Ann Neurol *78*, 710-721. 10.1002/ana.24497.
13. Trapp, B.D., and Stys, P.K. (2009). Virtual hypoxia and chronic necrosis of demyelinated axons in multiple sclerosis. Lancet Neurol *8*, 280-291. 10.1016/S1474-4422(09)70043-2.
14. Hagemeier, K., Bruck, W., and Kuhlmann, T. (2012). Multiple sclerosis - remyelination failure as a cause of disease progression. Histol Histopathol *27*, 277-287. 10.14670/HH-27.277.
15. Franklin, R.J., and Ffrench-Constant, C. (2008). Remyelination in the CNS: from biology to therapy. Nat Rev Neurosci *9*, 839-855. 10.1038/nrn2480.
16. Nave, K.A. (2010). Myelination and the trophic support of long axons. Nat Rev Neurosci *11*, 275-283. 10.1038/nrn2797.
17. Edgar, J.M., and Nave, K.A. (2009). The role of CNS glia in preserving axon function. Curr Opin Neurobiol *19*, 498-504. 10.1016/j.conb.2009.08.003.
18. De Stefano, N., Matthews, P.M., Fu, L., Narayanan, S., Stanley, J., Francis, G.S., Antel, J.P., and Arnold, D.L. (1998). Axonal damage correlates with disability in patients with relapsing-remitting multiple sclerosis. Results of a longitudinal magnetic resonance spectroscopy study. Brain *121 (Pt 8)*, 1469-1477. 10.1093/brain/121.8.1469.
19. Carassiti, D., Altmann, D.R., Petrova, N., Pakkenberg, B., Scaravilli, F., and Schmierer, K. (2018). Neuronal loss, demyelination and volume change in the multiple sclerosis neocortex. Neuropathol Appl Neurobiol *44*, 377-390. 10.1111/nan.12405.
20. Singh, S., Dallenga, T., Winkler, A., Roemer, S., Maruschak, B., Siebert, H., Bruck, W., and Stadelmann, C. (2017). Relationship of acute axonal damage, Wallerian degeneration, and clinical disability in multiple sclerosis. J Neuroinflammation *14*, 57. 10.1186/s12974-017-0831-8.
21. Magliozzi, R., Howell, O.W., Reeves, C., Roncaroli, F., Nicholas, R., Serafini, B., Aloisi, F., and Reynolds, R. (2010). A Gradient of neuronal loss and meningeal inflammation in multiple sclerosis. Ann Neurol *68*, 477-493. 10.1002/ana.22230.
22. Bodini, B., Veronese, M., Garcia-Lorenzo, D., Battaglini, M., Poirion, E., Chardain, A., Freeman, L., Louapre, C., Tchikviladze, M., Papeix, C., et al. (2016). Dynamic Imaging of Individual Remyelination Profiles in Multiple Sclerosis. Ann Neurol *79*, 726-738. 10.1002/ana.24620.
23. Kornek, B., Storch, M.K., Weissert, R., Wallstroem, E., Stefferl, A., Olsson, T., Linington, C., Schmidbauer, M., and Lassmann, H. (2000). Multiple sclerosis and chronic autoimmune encephalomyelitis: a comparative quantitative study of axonal injury in active, inactive, and remyelinated lesions. Am J Pathol *157*, 267-276. 10.1016/S0002-9440(10)64537-3.
24. Franklin, R.J., ffrench-Constant, C., Edgar, J.M., and Smith, K.J. (2012). Neuroprotection and repair in multiple sclerosis. Nat Rev Neurol *8*, 624-634. 10.1038/nrneurol.2012.200.

25. Trapp, B.D., Peterson, J., Ransohoff, R.M., Rudick, R., Mork, S., and Bo, L. (1998). Axonal transection in the lesions of multiple sclerosis. N Engl J Med *338*, 278-285. 10.1056/NEJM199801293380502.
26. Kuhlmann, T., Lingfeld, G., Bitsch, A., Schuchardt, J., and Bruck, W. (2002). Acute axonal damage in multiple sclerosis is most extensive in early disease stages and decreases over time. Brain *125*, 2202-2212. 10.1093/brain/awf235.
27. Bitsch, A., Schuchardt, J., Bunkowski, S., Kuhlmann, T., and Bruck, W. (2000). Acute axonal injury in multiple sclerosis. Correlation with demyelination and inflammation. Brain *123 (Pt 6)*, 1174-1183. 10.1093/brain/123.6.1174.
28. Ferguson, B., Matyszak, M.K., Esiri, M.M., and Perry, V.H. (1997). Axonal damage in acute multiple sclerosis lesions. Brain *120 (Pt 3)*, 393-399. 10.1093/brain/120.3.393.
29. Miller, B.R., Press, C., Daniels, R.W., Sasaki, Y., Milbrandt, J., and DiAntonio, A. (2009). A dual leucine kinase-dependent axon self-destruction program promotes Wallerian degeneration. Nat Neurosci *12*, 387-389. 10.1038/nn.2290.
30. Xu, Z., Maroney, A.C., Dobrzanski, P., Kukekov, N.V., and Greene, L.A. (2001). The MLK family mediates c-Jun N-terminal kinase activation in neuronal apoptosis. Mol Cell Biol *21*, 4713-4724. 10.1128/MCB.21.14.4713-4724.2001.
31. Huntwork-Rodriguez, S., Wang, B., Watkins, T., Ghosh, A.S., Pozniak, C.D., Bustos, D., Newton, K., Kirkpatrick, D.S., and Lewcock, J.W. (2013). JNK-mediated phosphorylation of DLK suppresses its ubiquitination to promote neuronal apoptosis. J Cell Biol *202*, 747-763. 10.1083/jcb.201303066.
32. Itoh, T., Horiuchi, M., Ikeda, R.H., Jr., Xu, J., Bannerman, P., Pleasure, D., Penninger, J.M., Tournier, C., and Itoh, A. (2014). ZPK/DLK and MKK4 form the critical gateway to axotomy-induced motoneuron death in neonates. J Neurosci *34*, 10729-10742. 10.1523/JNEUROSCI.0539-14.2014.
33. Hirai, S., Izawa, M., Osada, S., Spyrou, G., and Ohno, S. (1996). Activation of the JNK pathway by distantly related protein kinases, MEKK and MUK. Oncogene *12*, 641-650.
34. Ghosh, A.S., Wang, B., Pozniak, C.D., Chen, M., Watts, R.J., and Lewcock, J.W. (2011). DLK induces developmental neuronal degeneration via selective regulation of proapoptotic JNK activity. J Cell Biol *194*, 751-764. 10.1083/jcb.201103153.
35. Syc-Mazurek, S.B., Rausch, R.L., Fernandes, K.A., Wilson, M.P., and Libby, R.T. (2018). Mkk4 and Mkk7 are important for retinal development and axonal injury-induced retinal ganglion cell death. Cell Death Dis *9*, 1095. 10.1038/s41419-018-1079-7.
36. Le Pichon, C.E., Meilandt, W.J., Dominguez, S., Solanoy, H., Lin, H., Ngu, H., Gogineni, A., Sengupta Ghosh, A., Jiang, Z., Lee, S.H., et al. (2017). Loss of dual leucine zipper kinase signaling is protective in animal models of neurodegenerative disease. Sci Transl Med *9*. 10.1126/scitranslmed.aag0394.
37. Watkins, T.A., Wang, B., Huntwork-Rodriguez, S., Yang, J., Jiang, Z., Eastham-Anderson, J., Modrusan, Z., Kaminker, J.S., Tessier-Lavigne, M., and Lewcock, J.W. (2013). DLK initiates a transcriptional program that couples apoptotic and regenerative responses to axonal injury. Proc Natl Acad Sci U S A *110*, 4039-4044. 10.1073/pnas.1211074110.
38. Welsbie, D.S., Yang, Z., Ge, Y., Mitchell, K.L., Zhou, X., Martin, S.E., Berlinicke, C.A., Hackler, L., Jr., Fuller, J., Fu, J., et al. (2013). Functional genomic screening identifies dual leucine zipper kinase as a key mediator of retinal ganglion cell death. Proc Natl Acad Sci U S A *110*, 4045-4050. 10.1073/pnas.1211284110.

39. Bujalka, H., Koenning, M., Jackson, S., Perreau, V.M., Pope, B., Hay, C.M., Mitew, S., Hill, A.F., Lu, Q.R., Wegner, M., et al. (2013). MYRF is a membrane-associated transcription factor that autoproteolytically cleaves to directly activate myelin genes. PLoS Biol *11*, e1001625. 10.1371/journal.pbio.1001625.
40. Emery, B., Agalliu, D., Cahoy, J.D., Watkins, T.A., Dugas, J.C., Mulinyawe, S.B., Ibrahim, A., Ligon, K.L., Rowitch, D.H., and Barres, B.A. (2009). Myelin gene regulatory factor is a critical transcriptional regulator required for CNS myelination. Cell *138*, 172-185. 10.1016/j.cell.2009.04.031.
41. Hornig, J., Frob, F., Vogl, M.R., Hermans-Borgmeyer, I., Tamm, E.R., and Wegner, M. (2013). The transcription factors Sox10 and Myrf define an essential regulatory network module in differentiating oligodendrocytes. PLoS Genet *9*, e1003907. 10.1371/journal.pgen.1003907.
42. Koenning, M., Jackson, S., Hay, C.M., Faux, C., Kilpatrick, T.J., Willingham, M., and Emery, B. (2012). Myelin gene regulatory factor is required for maintenance of myelin and mature oligodendrocyte identity in the adult CNS. J Neurosci *32*, 12528-12542. 10.1523/JNEUROSCI.1069-12.2012.
43. Hartley, M.D., Banerji, T., Tagge, I.J., Kirkemo, L.L., Chaudhary, P., Calkins, E., Galipeau, D., Shokat, M.D., DeBell, M.J., Van Leuven, S., et al. (2019). Myelin repair stimulated by CNS-selective thyroid hormone action. JCI Insight *4*. 10.1172/jci.insight.126329.
44. Duncan, G.J., Plemel, J.R., Assinck, P., Manesh, S.B., Muir, F.G.W., Hirata, R., Berson, M., Liu, J., Wegner, M., Emery, B., et al. (2017). Myelin regulatory factor drives remyelination in multiple sclerosis. Acta Neuropathol *134*, 403-422. 10.1007/s00401-017-1741-7.
45. McKenzie, I.A., Ohayon, D., Li, H., de Faria, J.P., Emery, B., Tohyama, K., and Richardson, W.D. (2014). Motor skill learning requires active central myelination. Science *346*, 318-322. 10.1126/science.1254960.
46. Gyllensten, L., and Malmfors, T. (1963). Myelinization of the optic nerve and its dependence on visual function--a quantitative investigation in mice. J Embryol Exp Morphol *11*, 255-266.
47. Fard, M.K., van der Meer, F., Sanchez, P., Cantuti-Castelvetri, L., Mandad, S., Jakel, S., Fornasiero, E.F., Schmitt, S., Ehrlich, M., Starost, L., et al. (2017). BCAS1 expression defines a population of early myelinating oligodendrocytes in multiple sclerosis lesions. Sci Transl Med *9*. 10.1126/scitranslmed.aam7816.
48. Hou, J., Zhou, Y., Cai, Z., Terekhova, M., Swain, A., Andhey, P.S., Guimaraes, R.M., Ulezko Antonova, A., Qiu, T., Sviben, S., et al. (2023). Transcriptomic atlas and interaction networks of brain cells in mouse CNS demyelination and remyelination. Cell Rep *42*, 112293. 10.1016/j.celrep.2023.112293.
49. Pandey, S., Shen, K., Lee, S.H., Shen, Y.A., Wang, Y., Otero-Garcia, M., Kotova, N., Vito, S.T., Laufer, B.I., Newton, D.F., et al. (2022). Disease-associated oligodendrocyte responses across neurodegenerative diseases. Cell Rep *40*, 111189. 10.1016/j.celrep.2022.111189.
50. Park, H., Cho, B., Kim, H., Saito, T., Saido, T.C., Won, K.J., and Kim, J. (2023). Single-cell RNA-sequencing identifies disease-associated oligodendrocytes in male APP NL-G-F and 5XFAD mice. Nat Commun *14*, 802. 10.1038/s41467-023-36519-8.

51. Chistiakov, D.A., Killingsworth, M.C., Myasoedova, V.A., Orekhov, A.N., and Bobryshev, Y.V. (2017). CD68/macrosialin: not just a histochemical marker. Lab Invest *97*, 4-13. 10.1038/labinvest.2016.116.
52. Hammond, T.R., Dufort, C., Dissing-Olesen, L., Giera, S., Young, A., Wysoker, A., Walker, A.J., Gergits, F., Segel, M., Nemesh, J., et al. (2019). Single-Cell RNA Sequencing of Microglia throughout the Mouse Lifespan and in the Injured Brain Reveals Complex Cell-State Changes. Immunity *50*, 253-271 e256. 10.1016/j.immuni.2018.11.004.
53. Wlodarczyk, A., Holtman, I.R., Krueger, M., Yogev, N., Bruttger, J., Khorooshi, R., Benmamar-Badel, A., de Boer-Bergsma, J.J., Martin, N.A., Karram, K., et al. (2017). A novel microglial subset plays a key role in myelinogenesis in developing brain. EMBO J *36*, 3292-3308. 10.15252/embj.201696056.
54. Connor, J.R., and Menzies, S.L. (1996). Relationship of iron to oligodendrocytes and myelination. Glia *17*, 83-93. 10.1002/(SICI)1098-1136(199606)17:2<83::AID-GLIA1>3.0.CO;2-7.
55. Nikic, I., Merkler, D., Sorbara, C., Brinkoetter, M., Kreutzfeldt, M., Bareyre, F.M., Bruck, W., Bishop, D., Misgeld, T., and Kerschensteiner, M. (2011). A reversible form of axon damage in experimental autoimmune encephalomyelitis and multiple sclerosis. Nat Med *17*, 495-499. 10.1038/nm.2324.
56. Schaffner, E., Bosch-Queralt, M., Edgar, J.M., Lehning, M., Strauss, J., Fleischer, N., Kungl, T., Wieghofer, P., Berghoff, S.A., Reinert, T., et al. (2023). Myelin insulation as a risk factor for axonal degeneration in autoimmune demyelinating disease. Nat Neurosci *26*, 1218-1228. 10.1038/s41593-023-01366-9.
57. Abdelhak, A., Kuhle, J., and Green, A.J. (2023). Challenges and Opportunities for the Promising Biomarker Blood Neurofilament Light Chain. JAMA Neurol *80*, 542-543. 10.1001/jamaneurol.2023.0394.
58. Shaw, G., Madorsky, I., Li, Y., Wang, Y., Jorgensen, M., Rana, S., and Fuller, D.D. (2023). Uman-type neurofilament light antibodies are effective reagents for the imaging of neurodegeneration. Brain Commun *5*, fcad067. 10.1093/braincomms/fcad067.
59. Kwong, J.M., Caprioli, J., and Piri, N. (2010). RNA binding protein with multiple splicing: a new marker for retinal ganglion cells. Invest Ophthalmol Vis Sci *51*, 1052-1058. 10.1167/iovs.09-4098.
60. Rodriguez, A.R., de Sevilla Muller, L.P., and Brecha, N.C. (2014). The RNA binding protein RBPMS is a selective marker of ganglion cells in the mammalian retina. J Comp Neurol *522*, 1411-1443. 10.1002/cne.23521.
61. Larhammar, M., Huntwork-Rodriguez, S., Jiang, Z., Solanoy, H., Sengupta Ghosh, A., Wang, B., Kaminker, J.S., Huang, K., Eastham-Anderson, J., Siu, M., et al. (2017). Dual leucine zipper kinase-dependent PERK activation contributes to neuronal degeneration following insult. Elife *6*. 10.7554/eLife.20725.
62. Fernandes, K.A., Harder, J.M., Kim, J., and Libby, R.T. (2013). JUN regulates early transcriptional responses to axonal injury in retinal ganglion cells. Exp Eye Res *112*, 106-117. 10.1016/j.exer.2013.04.021.
63. Holland, S.M., Collura, K.M., Ketschek, A., Noma, K., Ferguson, T.A., Jin, Y., Gallo, G., and Thomas, G.M. (2016). Palmitoylation controls DLK localization, interactions and activity to ensure effective axonal injury signaling. Proc Natl Acad Sci U S A *113*, 763-768. 10.1073/pnas.1514123113.

64. Niu, J., Holland, S.M., Ketschek, A., Collura, K.M., Hesketh, N.L., Hayashi, T., Gallo, G., and Thomas, G.M. (2022). Palmitoylation couples the kinases DLK and JNK3 to facilitate prodegenerative axon-to-soma signaling. Sci Signal *15*, eabh2674. 10.1126/scisignal.abh2674.
65. Welsbie, D.S., Ziogas, N.K., Xu, L., Kim, B.J., Ge, Y., Patel, A.K., Ryu, J., Lehar, M., Alexandris, A.S., Stewart, N., et al. (2019). Targeted disruption of dual leucine zipper kinase and leucine zipper kinase promotes neuronal survival in a model of diffuse traumatic brain injury. Mol Neurodegener *14*, 44. 10.1186/s13024-019-0345-1.
66. Craig, R.A., 2nd, Fox, B.M., Hu, C., Lexa, K.W., Osipov, M., Thottumkara, A.P., Larhammar, M., Miyamoto, T., Rana, A., Kane, L.A., et al. (2022). Discovery of Potent and Selective Dual Leucine Zipper Kinase/Leucine Zipper-Bearing Kinase Inhibitors with Neuroprotective Properties in In Vitro and In Vivo Models of Amyotrophic Lateral Sclerosis. J Med Chem *65*, 16290-16312. 10.1021/acs.jmedchem.2c01056.
67. Patel, S., Harris, S.F., Gibbons, P., Deshmukh, G., Gustafson, A., Kellar, T., Lin, H., Liu, X., Liu, Y., Liu, Y., et al. (2015). Scaffold-Hopping and Structure-Based Discovery of Potent, Selective, And Brain Penetrant N-(1H-Pyrazol-3-yl)pyridin-2-amine Inhibitors of Dual Leucine Zipper Kinase (DLK, MAP3K12). J Med Chem *58*, 8182-8199. 10.1021/acs.jmedchem.5b01072.
68. Patel, S., Cohen, F., Dean, B.J., De La Torre, K., Deshmukh, G., Estrada, A.A., Ghosh, A.S., Gibbons, P., Gustafson, A., Huestis, M.P., et al. (2015). Discovery of dual leucine zipper kinase (DLK, MAP3K12) inhibitors with activity in neurodegeneration models. J Med Chem *58*, 401-418. 10.1021/jm5013984.
69. Summers, D.W., Frey, E., Walker, L.J., Milbrandt, J., and DiAntonio, A. (2020). DLK Activation Synergizes with Mitochondrial Dysfunction to Downregulate Axon Survival Factors and Promote SARM1-Dependent Axon Degeneration. Mol Neurobiol *57*, 1146-1158. 10.1007/s12035-019-01796-2.
70. Welsbie, D.S., Mitchell, K.L., Jaskula-Ranga, V., Sluch, V.M., Yang, Z., Kim, J., Buehler, E., Patel, A., Martin, S.E., Zhang, P.W., et al. (2017). Enhanced Functional Genomic Screening Identifies Novel Mediators of Dual Leucine Zipper Kinase-Dependent Injury Signaling in Neurons. Neuron *94*, 1142-1154 e1146. 10.1016/j.neuron.2017.06.008.
71. Chapman, T.W., Olveda, G.E., Bame, X., Pereira, E., and Hill, R.A. (2023). Oligodendrocyte death initiates synchronous remyelination to restore cortical myelin patterns in mice. Nat Neurosci *26*, 555-569. 10.1038/s41593-023-01271-1.
72. Xiao, L., Ohayon, D., McKenzie, I.A., Sinclair-Wilson, A., Wright, J.L., Fudge, A.D., Emery, B., Li, H., and Richardson, W.D. (2016). Rapid production of new oligodendrocytes is required in the earliest stages of motor-skill learning. Nat Neurosci *19*, 1210-1217. 10.1038/nn.4351.
73. Steadman, P.E., Xia, F., Ahmed, M., Mocle, A.J., Penning, A.R.A., Geraghty, A.C., Steenland, H.W., Monje, M., Josselyn, S.A., and Frankland, P.W. (2020). Disruption of Oligodendrogenesis Impairs Memory Consolidation in Adult Mice. Neuron *105*, 150-164 e156. 10.1016/j.neuron.2019.10.013.
74. Pan, S., Mayoral, S.R., Choi, H.S., Chan, J.R., and Kheirbek, M.A. (2020). Preservation of a remote fear memory requires new myelin formation. Nat Neurosci *23*, 487-499. 10.1038/s41593-019-0582-1.

75. Kotter, M.R., Li, W.W., Zhao, C., and Franklin, R.J. (2006). Myelin impairs CNS remyelination by inhibiting oligodendrocyte precursor cell differentiation. J Neurosci *26*, 328-332. 10.1523/JNEUROSCI.2615-05.2006.
76. Miron, V.E., Boyd, A., Zhao, J.W., Yuen, T.J., Ruckh, J.M., Shadrach, J.L., van Wijngaarden, P., Wagers, A.J., Williams, A., Franklin, R.J.M., and Ffrench-Constant, C. (2013). M2 microglia and macrophages drive oligodendrocyte differentiation during CNS remyelination. Nat Neurosci *16*, 1211-1218. 10.1038/nn.3469.
77. Ruckh, J.M., Zhao, J.W., Shadrach, J.L., van Wijngaarden, P., Rao, T.N., Wagers, A.J., and Franklin, R.J. (2012). Rejuvenation of regeneration in the aging central nervous system. Cell Stem Cell *10*, 96-103. 10.1016/j.stem.2011.11.019.
78. Foote, A.K., and Blakemore, W.F. (2005). Inflammation stimulates remyelination in areas of chronic demyelination. Brain *128*, 528-539. 10.1093/brain/awh417.
79. Safaiyan, S., Besson-Girard, S., Kaya, T., Cantuti-Castelvetri, L., Liu, L., Ji, H., Schifferer, M., Gouna, G., Usifo, F., Kannaiyan, N., et al. (2021). White matter aging drives microglial diversity. Neuron *109*, 1100-1117 e1110. 10.1016/j.neuron.2021.01.027.
80. Cantuti-Castelvetri, L., Fitzner, D., Bosch-Queralt, M., Weil, M.T., Su, M., Sen, P., Ruhwedel, T., Mitkovski, M., Trendelenburg, G., Lutjohann, D., et al. (2018). Defective cholesterol clearance limits remyelination in the aged central nervous system. Science *359*, 684-688. 10.1126/science.aan4183.
81. Berghoff, S.A., Spieth, L., Sun, T., Hosang, L., Schlaphoff, L., Depp, C., Duking, T., Winchenbach, J., Neuber, J., Ewers, D., et al. (2021). Microglia facilitate repair of demyelinated lesions via post-squalene sterol synthesis. Nat Neurosci *24*, 47-60. 10.1038/s41593-020-00757-6.
82. Kutzelnigg, A., Lucchinetti, C.F., Stadelmann, C., Bruck, W., Rauschka, H., Bergmann, M., Schmidbauer, M., Parisi, J.E., and Lassmann, H. (2005). Cortical demyelination and diffuse white matter injury in multiple sclerosis. Brain *128*, 2705-2712. 10.1093/brain/awh641.
83. Ricigliano, V.A.G., Tonietto, M., Hamzaoui, M., Poirion, E., Lazzarotto, A., Bottlaender, M., Gervais, P., Maillart, E., Stankoff, B., and Bodini, B. (2022). Spontaneous remyelination in lesions protects the integrity of surrounding tissues over time in multiple sclerosis. Eur J Neurol *29*, 1719-1729. 10.1111/ene.15285.
84. Tonietto, M., Poirion, E., Lazzarotto, A., Ricigliano, V., Papeix, C., Bottlaender, M., Bodini, B., and Stankoff, B. (2023). Periventricular remyelination failure in multiple sclerosis: a substrate for neurodegeneration. Brain *146*, 182-194. 10.1093/brain/awac334.
85. Mei, F., Lehmann-Horn, K., Shen, Y.A., Rankin, K.A., Stebbins, K.J., Lorrain, D.S., Pekarek, K., S, A.S., Xiao, L., Teuscher, C., et al. (2016). Accelerated remyelination during inflammatory demyelination prevents axonal loss and improves functional recovery. Elife *5*. 10.7554/eLife.18246.
86. Peterson, J.W., Bo, L., Mork, S., Chang, A., and Trapp, B.D. (2001). Transected neurites, apoptotic neurons, and reduced inflammation in cortical multiple sclerosis lesions. Ann Neurol *50*, 389-400. 10.1002/ana.1123.
87. Trapp, B.D., Vignos, M., Dudman, J., Chang, A., Fisher, E., Staugaitis, S.M., Battapady, H., Mork, S., Ontaneda, D., Jones, S.E., et al. (2018). Cortical neuronal densities and cerebral white matter demyelination in multiple sclerosis: a retrospective study. Lancet Neurol *17*, 870-884. 10.1016/S1474-4422(18)30245-X.

88. Somasundaram, P., Farley, M.M., Rudy, M.A., Stefanoff, D.G., Shah, M., Goli, P., Heo, J., Wang, S., Tran, N.M., and Watkins, T.A. (2023). Coordinated stimulation of axon regenerative and neurodegenerative transcriptional programs by Atf4 following optic nerve injury. bioRxiv. 10.1101/2023.03.29.534798.
89. Syc-Mazurek, S.B., Fernandes, K.A., Wilson, M.P., Shrager, P., and Libby, R.T. (2017). Together JUN and DDIT3 (CHOP) control retinal ganglion cell death after axonal injury. Mol Neurodegener *12*, 71. 10.1186/s13024-017-0214-8.
90. Harris, C.A., and Johnson, E.M., Jr. (2001). BH3-only Bcl-2 family members are coordinately regulated by the JNK pathway and require Bax to induce apoptosis in neurons. J Biol Chem *276*, 37754-37760. 10.1074/jbc.M104073200.
91. Levkovitch-Verbin, H., Quigley, H.A., Martin, K.R., Harizman, N., Valenta, D.F., Pease, M.E., and Melamed, S. (2005). The transcription factor c-jun is activated in retinal ganglion cells in experimental rat glaucoma. Exp Eye Res *80*, 663-670. 10.1016/j.exer.2004.11.016.
92. Buccarello, L., Dragotto, J., Hassanzadeh, K., Maccarone, R., Corbo, M., and Feligioni, M. (2021). Retinal ganglion cell loss in an ex vivo mouse model of optic nerve cut is prevented by curcumin treatment. Cell Death Discov *7*, 394. 10.1038/s41420-021-00760-1.
93. Isenmann, S., and Bahr, M. (1997). Expression of c-Jun protein in degenerating retinal ganglion cells after optic nerve lesion in the rat. Exp Neurol *147*, 28-36. 10.1006/exnr.1997.6585.
94. Tian, R., Abarientos, A., Hong, J., Hashemi, S.H., Yan, R., Drager, N., Leng, K., Nalls, M.A., Singleton, A.B., Xu, K., et al. (2021). Genome-wide CRISPRi/a screens in human neurons link lysosomal failure to ferroptosis. Nat Neurosci *24*, 1020-1034. 10.1038/s41593-021-00862-0.
95. Jacobi, A., Tran, N.M., Yan, W., Benhar, I., Tian, F., Schaffer, R., He, Z., and Sanes, J.R. (2022). Overlapping transcriptional programs promote survival and axonal regeneration of injured retinal ganglion cells. Neuron *110*, 2625-2645 e2627. 10.1016/j.neuron.2022.06.002.
96. Kiryu-Seo, S., Ohno, N., Kidd, G.J., Komuro, H., and Trapp, B.D. (2010). Demyelination increases axonal stationary mitochondrial size and the speed of axonal mitochondrial transport. J Neurosci *30*, 6658-6666. 10.1523/JNEUROSCI.5265-09.2010.
97. Zambonin, J.L., Zhao, C., Ohno, N., Campbell, G.R., Engeham, S., Ziabreva, I., Schwarz, N., Lee, S.E., Frischer, J.M., Turnbull, D.M., et al. (2011). Increased mitochondrial content in remyelinated axons: implications for multiple sclerosis. Brain *134*, 1901-1913. 10.1093/brain/awr110.
98. Gomez-Deza, J.J., Nebiyou, M., Alkaslasi, M.R., Somasundaran, P., Slavutsky, A.L., Ward, M.E., Watkins, T.A., and Le Pichon, C.E. (2023). DLK-dependent mitochondrial fission drives axon degeneration and neuronal cell death. bioRxiv. 10.1101/2023.01.30.526132.
99. Liesa, M., and Shirihai, O.S. (2013). Mitochondrial dynamics in the regulation of nutrient utilization and energy expenditure. Cell Metab *17*, 491-506. 10.1016/j.cmet.2013.03.002.
100. Gomes, L.C., Di Benedetto, G., and Scorrano, L. (2011). During autophagy mitochondria elongate, are spared from degradation and sustain cell viability. Nat Cell Biol *13*, 589-598. 10.1038/ncb2220.

101. Duncan, G.J., Simkins, T.J., and Emery, B. (2021). Neuron-Oligodendrocyte Interactions in the Structure and Integrity of Axons. Front Cell Dev Biol *9*, 653101. 10.3389/fcell.2021.653101.
102. Friese, M.A., Schattling, B., and Fugger, L. (2014). Mechanisms of neurodegeneration and axonal dysfunction in multiple sclerosis. Nat Rev Neurol *10*, 225-238. 10.1038/nrneurol.2014.37.
103. Frank, S., Gaume, B., Bergmann-Leitner, E.S., Leitner, W.W., Robert, E.G., Catez, F., Smith, C.L., and Youle, R.J. (2001). The role of dynamin-related protein 1, a mediator of mitochondrial fission, in apoptosis. Dev Cell *1*, 515-525. 10.1016/s1534-5807(01)00055-7.
104. Summers, D.W., Milbrandt, J., and DiAntonio, A. (2018). Palmitoylation enables MAPK-dependent proteostasis of axon survival factors. Proc Natl Acad Sci U S A *115*, E8746-E8754. 10.1073/pnas.1806933115.
105. Katz, J.S., Rothstein, J.D., Cudkowicz, M.E., Genge, A., Oskarsson, B., Hains, A.B., Chen, C., Galanter, J., Burgess, B.L., Cho, W., et al. (2022). A Phase 1 study of GDC-0134, a dual leucine zipper kinase inhibitor, in ALS. Ann Clin Transl Neurol *9*, 50-66. 10.1002/acn3.51491.
106. Doerflinger, N.H., Macklin, W.B., and Popko, B. (2003). Inducible site-specific recombination in myelinating cells. Genesis *35*, 63-72. 10.1002/gene.10154.
107. Platt, R.J., Chen, S., Zhou, Y., Yim, M.J., Swiech, L., Kempton, H.R., Dahlman, J.E., Parnas, O., Eisenhaure, T.M., Jovanovic, M., et al. (2014). CRISPR-Cas9 knockin mice for genome editing and cancer modeling. Cell *159*, 440-455. 10.1016/j.cell.2014.09.014.
108. Young, K.M., Psachoulia, K., Tripathi, R.B., Dunn, S.J., Cossell, L., Attwell, D., Tohyama, K., and Richardson, W.D. (2013). Oligodendrocyte dynamics in the healthy adult CNS: evidence for myelin remodeling. Neuron *77*, 873-885. 10.1016/j.neuron.2013.01.006.
109. Baltan, S., Besancon, E.F., Mbow, B., Ye, Z., Hamner, M.A., and Ransom, B.R. (2008). White matter vulnerability to ischemic injury increases with age because of enhanced excitotoxicity. J Neurosci *28*, 1479-1489. 10.1523/JNEUROSCI.5137-07.2008.
110. Stys, P.K., Ransom, B.R., and Waxman, S.G. (1991). Compound action potential of nerve recorded by suction electrode: a theoretical and experimental analysis. Brain Res *546*, 18-32. 10.1016/0006-8993(91)91154-s.
111. Cordano, C., Sin, J.H., Timmons, G., Yiu, H.H., Stebbins, K., Guglielmetti, C., Cruz-Herranz, A., Xin, W., Lorrain, D., Chan, J.R., and Green, A.J. (2022). Validating visual evoked potentials as a preclinical, quantitative biomarker for remyelination efficacy. Brain *145*, 3943-3952. 10.1093/brain/awac207.
112. Calkins, E., Pocius, E., Marracci, G., and Chaudhary, P. (2020). A microwave method for plastic embedding of nervous tissue for light and electron microscopy. Heliyon *6*, e03036. 10.1016/j.heliyon.2019.e03036.
113. Satija, R., Farrell, J.A., Gennert, D., Schier, A.F., and Regev, A. (2015). Spatial reconstruction of single-cell gene expression data. Nat Biotechnol *33*, 495-502. 10.1038/nbt.3192.
114. Young, M.D., and Behjati, S. (2020). SoupX removes ambient RNA contamination from droplet-based single-cell RNA sequencing data. Gigascience *9*. 10.1093/gigascience/giaa151.

115. Hafemeister, C., and Satija, R. (2019). Normalization and variance stabilization of single-cell RNA-seq data using regularized negative binomial regression. Genome Biol *20*, 296. 10.1186/s13059-019-1874-1.
116. Yu, G., Wang, L.G., Han, Y., and He, Q.Y. (2012). clusterProfiler: an R package for comparing biological themes among gene clusters. OMICS *16*, 284-287. 10.1089/omi.2011.0118.
117. Xiang, X., Corsi, G.I., Anthon, C., Qu, K., Pan, X., Liang, X., Han, P., Dong, Z., Liu, L., Zhong, J., et al. (2021). Enhancing CRISPR-Cas9 gRNA efficiency prediction by data integration and deep learning. Nat Commun *12*, 3238. 10.1038/s41467-021-23576-0.
118. Brinkman, E.K., Chen, T., Amendola, M., and van Steensel, B. (2014). Easy quantitative assessment of genome editing by sequence trace decomposition. Nucleic Acids Res *42*, e168. 10.1093/nar/gku936.
119. Swiech, L., Heidenreich, M., Banerjee, A., Habib, N., Li, Y., Trombetta, J., Sur, M., and Zhang, F. (2015). In vivo interrogation of gene function in the mammalian brain using CRISPR-Cas9. Nat Biotechnol *33*, 102-106. 10.1038/nbt.3055.
120. Zhang, J.P., Li, X.L., Neises, A., Chen, W., Hu, L.P., Ji, G.Z., Yu, J.Y., Xu, J., Yuan, W.P., Cheng, T., and Zhang, X.B. (2016). Different Effects of sgRNA Length on CRISPR-mediated Gene Knockout Efficiency. Sci Rep *6*, 28566. 10.1038/srep28566.

Figure Legends

Figure 1. Myrf$^{\Delta iSox10}$ mice undergo CNS demyelination with limited remyelination.

(A) Transgenic strategy to induce demyelination with the aim of permitting (Myrf$^{\Delta iPlp1}$ mice) or inhibiting (Myrf$^{\Delta iSox10}$ mice) remyelination.

(B) Timeline of tamoxifen administration, demyelination and remyelination in Myrf$^{\Delta iPlp1}$ and Myrf$^{\Delta iSox10}$ mice.

(C) Electron micrographs of the optic nerve of Myrf$^{fl/fl}$, Myrf$^{\Delta iPlp1}$ and Myrf$^{\Delta iSox10}$ mice at 10-weeks post-tamoxifen (TAM) and of Myrf$^{\Delta iPlp1}$ mice at 20-weeks post-tamoxifen.

(D) Quantification of the percentage of myelinated axons in the optic nerve. There is a statistically significant decline in the percentage of axons myelinated in Myrf$^{\Delta iPlp1}$ and Myrf$^{\Delta iSox10}$ relative to Myrf$^{fl/fl}$ ($p < 0.0001$). Myrf$^{\Delta iPLP}$ have more myelinated axons than Myrf$^{\Delta iSox10}$ mice at 10 weeks post tamoxifen ($p < 0.0001$). Myrf$^{\Delta iPlp1}$ mice have and increased myelinated axons week at 20 weeks relative to 10 weeks post tamoxifen ($p = 0.0036$).

(E) Optic nerve cross sections stained for MBP (myelin) and BCAS1 (new oligodendrocytes/myelin).

(F) Percentage of optic nerve that is BCAS1+. At 10 weeks post tamoxifen Myrf$^{\Delta iPlp1}$ mice have increased BCAS1 relative to Myrf$^{fl/fl}$ mice ($p < 0.0001$) and Myrf$^{\Delta iSox10}$ mice ($p < 0.0001$). BCAS1 expression is reduced by 20 weeks post-tamoxifen relative to 10 weeks in Myrf$^{\Delta iPlp1}$ mice ($p = 0.0274$).

(G) Example CAPs from the optic nerve. $Myrf^{fl/fl}$ control mice have three distinct peaks, whereas $Myrf^{\Delta iplp1}$ and $Myrf^{\Delta iSox10}$ only have two definable peaks.

(H) CAP latency during de- and remyelination. Both $Myrf^{\Delta iPlp1}$ ($p = 0.0019$) and $Myrf^{\Delta iSox10}$ ($p < 0.0001$) mice have increased latency at 10 and 20 weeks post-tamoxifen relative to non-demyelinated $Myrf^{fl/fl}$ mice. $Myrf^{\Delta iPlp1}$ have lower latency relative to $Myrf^{\Delta iSox10}$ at week 10 post tamoxifen ($p = 0.0151$).

(I) CAP area during de- and remyelination. Both $Myrf^{\Delta iPlp1}$ and $Myrf^{\Delta iSox10}$ mice have increased latency at 10 ($Myrf^{\Delta iPlp1}$, $p = 0.0026$ and $Myrf^{\Delta iSox10}$ $p = 0.0005$) and 20 weeks post-tamoxifen ($Myrf^{\Delta iPlp1}$ $p = 0.0005$) relative $Myrf^{fl/fl}$ mice.

(L) VEPs measured over time. At 10 weeks post-tamoxifen both $Myrf^{\Delta iPlp1}$ ($p = 0.0030$) and $Myrf^{\Delta iSox10}$ ($p < 0.0001$) differed from $Myrf^{fl/fl}$ and $Myrf^{\Delta iPlp1}$ had decreased latency relative to $Myrf^{\Delta iSox10}$ ($p< 0.0209$). By 20 weeks post-tamoxifen, latencies of $Myrf^{\Delta iPlp1}$ mice are indistinguishable from controls.

Scale bar is 1µm in (C), 50 µm in (E). Two-way ANOVA with Tukey's post hoc in (D), (F), (H), and (I). Mixed model with Tukey's *post hoc* in (L). NA = Not applicable.

Figure 2. Differentiation of remyelinating oligodendrocytes is blocked in $Myrf^{\Delta iSox10}$ mice following demyelination.

(A) Schematic of approach used to isolate and sequence nuclei from the optic nerve.

(B) Uniform manifold approximation and projection (UMAP) of 49,806 nuclei separating into 14 distinct clusters. COP = committed oligodendrocyte precursor cells, NFOL = newly-formed OL, MFOLs = myelin-forming OLs, MOLs = mature OLs, KOOL = knockout OLs, VLMC = vascular and leptomeningeal cells, ABC = arachnoid barrier cells.

(C) Dotplot showing cluster-specific markers.

(D) UMAP displaying expression of key markers of the OL lineage (*Sox10*), OPCs (*Pdgfra*), COP1s (*Gpr17*), NFOLs (*Tcf7l2*), MFOLs (*Mobp*) and MOLs *(Anln, Mobp*).

(E) UMAP of OL lineage cell nuclei broken down by genotype.

(F) Stacked bargraph showing the proportions of oligodendroglial cell clusters across genotypes. The KOOL population is specific to the $Myrf^{\Delta iPlp1}$ and $Myrf^{\Delta iSox10}$ mice. $Myrf^{\Delta iPlp1}$ lack MOLs and show expanded numbers of COPs, NFOLs and MFOLs. The NFOL, MFOL and MOL populations are essentially absent in $Myrf^{\Delta iSox10}$ mice.

(G) Selected violin plots for transcripts expressed in OLs across genotypes. $Myrf^{\Delta iSox10}$ mice do not have nuclei that express late stage OL markers and myelin genes.

(H) Optic nerve cross sections stained with the OL lineage marker, OLIG2 along with PDGFRα expressed in OPCs, and CC1 in OLs.

(I) The density of OLIG2+PDGFRα+ OPCs increases in both Myrf$^{\Delta iPlp1}$ ($p = 0.0034$) and Myrf$^{\Delta iSox10}$ ($p < 0.0001$) mice at 10 weeks post-tamoxifen relative to Myrf$^{fl/fl}$ control mice, but do not differ from each other ($p = 0.1490$).

(J) The density of OLIG2+CC1+ OLs decreases in both in both Myrf$^{\Delta iPlp1}$ ($p = 0.0237$) and Myrf$^{\Delta iSox10}$ ($p < 0.0001$) at 10 weeks post-tamoxifen relative to Myrf$^{fl/fl}$ mice. There are more OLIG2+CC1+ OLs in Myrf$^{\Delta iPlp1}$ relative to Myrf$^{\Delta iSox10}$ at 10 weeks post tamoxifen ($p = 0.0002$).

Scale bar is 50 µm in (H). Two-way ANOVA with Tukey's *post hoc* in (I) and (J). NA = Not applicable.

Figure 3. Myrf$^{\Delta iSox10}$ mice have an expansion of a novel population of microglia/macrophages characterized by lipid binding and metabolism genes following demyelination.

(A) Optic nerve cross-sections stained with IBA1 for microglia/macrophages and the lysosomal marker CD68.

(B) IBA1+ microglia/macrophage are increased in density in Myrf$^{\Delta iPlp1}$ ($p < 0.0001$) and Myrf$^{\Delta iSox10}$ ($p < 0.0001$) relative to Myrf$^{fl/fl}$ mice, but do not differ from each other ($p = 0.8201$) at 10 weeks post-tamoxifen in the optic nerve. IBA1+ microglia macrophages are reduced in Myrf$^{\Delta iPlp1}$ by 20 weeks post-tamoxifen relative to 10 weeks ($p = 0.0151$), but still remain elevated over Myrf$^{fl/fl}$ mice ($p < 0.0001$).

(C) The percent of the optic nerve occupied by CD68 staining is increased in in Myrf$^{\Delta iPlp1}$ ($p = 0.0097$) and Myrf$^{\Delta iSox10}$ ($p = 0.0351$) relative to Myrf$^{fl/fl}$ mice, but do not differ from each other ($p > 0.9999$) at 10 weeks post-tamoxifen. At 20 weeks post-tamoxifen the percent of the optic nerve that is CD68+ remains elevated in Myrf$^{\Delta iPlp1}$ relative to Myrf$^{fl/fl}$ mice ($p = 0.0097$).

(D) UMAP plot of reclustered microglia/macrophages nuclei identifying five annotated subclusters (homeostatic microglia, barrier associated macrophages (BAM), disease-associated microglia/macrophages (DIM 1-3). n = 11,402 nuclei.

(E) UMAP of key subcluster transcripts enriched within microglial/macrophage population; pan microglial/macrophage marker (*Csf1r*), homeostatic microglia (*Siglech*), BAMs (*Cd163*), DIMs (*Ms4a7*), DIM2 (*Igf1*) and DIM3 (*Atp8b4*).

(F) Dotplot showing expression of sub-cluster specific markers.

(G) Selected violin plots for transcripts associated with activation in microglia/macrophage nuclei.

(H) Venn diagram depicting the number and overlap of upregulated genes in Myrf$^{\Delta iPlp1}$ and Myrf$^{\Delta iSox10}$ relative to Myrf$^{fl/fl}$.

(I) UMAP of microglia/macrophage lineage cell nuclei broken down by genotype.

(J) Stacked bargraph of microglia/macrophage subcluster composition by genotype. $Myrf^{fl/fl}$ mice don't have large proportion of DIM nuclei, whereas $Myrf^{\Delta iSox10}$ mice are enriched for DIM3 relative to $Myrf^{\Delta iPlp1}$.

(K) Volcano plot of key enriched transcripts in DIM3. Log_2(fold change) > 0.5 adjusted $p<0.05$. Wilcoxon rank-sum test.

(L) DIM3 gene ontology top six terms for molecular function.

(M) Violin plots showing expression of select lipid binding and metabolism genes in the microglia/macrophage lineage by genotype.

Scale bars 50 µm in (A). Two-way ANOVA with Tukey's *post hoc* in (B) and (C). NA = Not applicable.

Figure 4. Remyelination protects axons from damage and neurons from apoptosis.

(A) High magnification electron micrographs of the optic nerve with insets showing healthy axons in a', a'', a''' axons with accumulations, a'''' electron dense axons.

(B) The number of axons with accumulations increase in $Myrf^{\Delta iPlp1}$ ($p=0.0347$) and $Myrf^{\Delta iSox10}$ mice ($p = 0.0031$) relative to $Myrf^{fl/fl}$ at 10 weeks post-tamoxifen. By 20 weeks post tamoxifen, $Myrf^{\Delta iPlp1}$ do not statistically differ from $Myrf^{fl/fl}$ ($p = 0.3191$).

(C) Quantification of total axon number in the optic nerve of $Myrf^{fl/fl}$, $Myrf^{\Delta iPlp1}$ and $Myrf^{\Delta iSox10}$ mice.

(D) Serum neurofilament levels are increased at 10 weeks post-tamoxifen in both $Myrf^{\Delta iPlp1}$ and $Myrf^{\Delta iSox10}$ mice ($p < 0.0001$) but levels fall in $Myrf^{\Delta iPlp1}$ ($p = 0.0161$) by 20 weeks post-tamoxifen.

(E) Degenerative neurofilament light chain staining in the optic nerve of $Myrf^{fl/fl}$, $Myrf^{\Delta iPlp1}$ and $Myrf^{\Delta iSox10}$ mice at 10 weeks post tamoxifen.

(F) Overview of retinas with locations of cleaved caspase-3+ cells in the ganglion cell layer (GCL) indicated by black X. Boxed area is shown in (I).

(G) Density of cleaved caspase-3+ cells are increased in $Myrf^{\Delta iSox10}$ relative to $Myrf^{fl/fl}$ and $Myrf^{\Delta iPlp1}$ mice at 10- and 12-weeks post-tamoxifen ($p < 0.0001$).

(H) Density of cleaved caspase-3 and RBPMS double-labeled cells are increased in $Myrf^{\Delta iSox10}$ relative to $Myrf^{fl/fl}$ and $Myrf^{\Delta iPlp1}$ at 10 and 12 post tamoxifen ($p < 0.0001$).

(I) Colabeling between cleaved caspase-3 and RBPMS in the retina. RBPMS+ cells that are cleaved caspase-3 typically have low or no expression of RBPMS. Arrowheads indicate cleaved-caspase-3+ cells.

(J) RBPMS in the retina across genotypes.

(K) There is no statistically significant loss of RBPMS RGCs in $Myrf^{\Delta iPlp1}$ mice relative to $Myrf^{fl/fl}$ controls ($p > 0.05$ at all time points assessed).

(L) $Myrf^{\Delta iSox10}$ mice show a reduction in RBPMS+ RGCs at 12 weeks post-tamoxifen relative to $Myrf^{fl/fl}$ controls ($p = 0.0265$).

Scale bars are 1µm in (A), 50 µm (E), (I) and (J) and 500 µm (F). One-way ANOVA in (B) and (C) with Tukey's *post hoc* test. Two-way ANOVA with Tukey's *post hoc* test in (D), (G), (H) and Šidák's *post hoc* in (K) and (L). NA = Not applicable.

Figure 5: Chronic demyelination in $Myrf^{\Delta iSox10}$ leads to activation of the DLK/JNK/c-Jun pathway.

(A) Experimental schematic and images of laser microdissection of the ganglion cell layer of the retina.

(B) Heatmap of expression of RGC specific transcripts in the micro-dissected ganglion cell layer samples relative to whole retina.

(C) Heatmap of select transcripts activated by c-Jun/DLK signaling in the GCL between genotypes.

(D) RNAscope *in situ* hybridization in the retina at 10 weeks post-tamoxifen with probes against *Rbpms* and *Hrk*. Arrowheads indicate *Rbpms/Hrk* double-positive cells.

(E) RNAscope *in situ* hybridization in the retina at 10 weeks post-tamoxifen with probes against *Rbpms* and *Ecel1*. Arrowheads indicate *Rbpms/Ecel1* double-positive cells.

(F) Retina at 10 weeks post tamoxifen stained with phosphorylated (Ser63) c-Jun and Tuj1 (β3-tubulin). Boxed area shown in (H).

(G) Phosphorylated c-Jun is increased in $Myrf^{\Delta iPlp1}$ mice at 10, 12 and 20 weeks post-tamoxifen relative to $Myrf^{fl/fl}$ ($p = 0.0014$). The density of phosphorylated c-Jun+ cells is increased in $Myrf^{\Delta iSox10}$ relative to $Myrf^{fl/fl}$ and $Myrf^{\Delta iPlp1}$ at 10 and 12 weeks post-tamoxifen ($p < 0.0001$).

(H) Examples of phosphorylated c-Jun within Tuj1+ cells of $Myrf^{\Delta iSox10}$ mice. Arrowheads indicate colabeled cells.

(I) Examples of phosphorylated c-Jun within RBPMS+ cells of $Myrf^{\Delta iSox10}$ mice. Arrowheads indicate colabeled cells.

(J) Schematic of the DLK-mediated MAPK cascade ultimately activating c-Jun.

(K) Western blot of optic nerves for DLK, pMKK4 (S257/T261), MKK4, pJNK (T183/Y185), JNK, MOG and β-actin loading control from optic nerves of $Myrf^{fl/fl}$, $Myrf^{\Delta iPlp1}$, $Myrf^{\Delta iSox10}$ mice.

(L) Quantification of western blots. There is increased levels pMKK4 ($p = 0.0434$), pJNK ($p = 0.0072$), and total JNK ($p = 0.0034$) in $Myrf^{\Delta iSox10}$ mice 10 weeks post-tamoxifen relative to $Myrf^{fl/fl}$. MOG levels are reduced in $Myrf^{\Delta iSox10}$ mice ($p = 0.0038$) relative to $Myrf^{fl/fl}$.

(M) Quantification of western blots. There is increased JNK levels ($p = 0.0309$) and decreased MOG in $Myrf^{\Delta iPlp1}$ ($p = 0.0073$) mice relative to controls.

Scale bars are 50 µm in (A), (F), 10 µm in (D) and (E), and 5µm in (I). Two-way ANOVA with Tukey's posthoc test in (G), Student's T-test in (L) and (M). NA = Not applicable.

Figure 6: Pharmacological inhibition of DLK reduces c-Jun phosphorylation and blocks neuronal apoptosis in demyelinated Myrf$^{\Delta iSox10}$ mice.

(A) Schematic of the DLK MAPK cascade and timeline of GNE-3511 administration.

(B) Example retinal flatmount images of vehicle and GNE-3511 treated mice (Myrf$^{\Delta iSox10}$ and Myrf$^{fl/fl}$ controls) stained with phosphorylated c-Jun and RBPMS at 10 weeks post-tamoxifen.

(D) Overview of retinas with locations of cleaved caspase-3+ cells in the ganglion cell layer (GCL) indicated by black X.

(E) GNE-3511-treated Myrf$^{\Delta iSox10}$ mice show a significant reduction in the density of phosphorylated c-Jun positive RGCs relative to vehicle-treated Myrf$^{\Delta iSox10}$ and both vehicle-treated and GNE-3511-treated Myrf$^{fl/fl}$ mice ($p < 0.0001$).

(F) GNE-3511-treatment of Myrf$^{\Delta iSox10}$ mice at 10 weeks post-post tamoxifen leads to a reduction in cleaved caspase-3+ cells relative to vehicle-treated controls tamoxifen ($p = 0.0002$) and Myrf$^{fl/fl}$ mice ($p < 0.0001$).

(G) Cleaved caspase-3+ RBPMS+ cells are decreased in GNE-3511-treated Myrf$^{\Delta iSox10}$ relative to vehicle-treated mice at 10 weeks post-tamoxifen ($p = 0.0005$).

Scale bars are 500 µm in (C) and 50 µm in (B). Two-way ANOVA with Tukeys *post hoc* in (E), (F) and (G).

Figure 7: DLK is necessary for neuronal apoptosis following demyelination in Myrf$^{\Delta iSox10}$ mice.

(A) Schematic of AAV approach for CRISPR/Cas9-mediated knockout in retinal cells.

(B) Retina stained with phosphorylated c-Jun and m-Cherry 10 weeks post tamoxifen following treatment with sgLacZ/sgGFP or sgDLK/sgLZK on the opposite eye. Inlays are of boxed areas and scale bar is 5 µm in boxed areas.

(C) Representative images of phosphorylated c-Jun immunostaining in retinal flatmounts following administration of sgLacZ/sgGFP, sgDLK/sgDLK or sgDLK/sgLZK.

(D) Overview of retinas with locations of cleaved caspase-3+ cells in the GCL indicated by black X in viral-treated eyes.

(E) There is a reduction in the number of phosphorylated c-Jun cells within the GCL following sgDLK/sgDLK administration in Myrf$^{\Delta iSox10}$ mice ($p = 0.0080$). Connected lines indicate eyes from the same mouse.

(F) There is a reduction in the number of phosphorylated c-Jun cells within the GCL following sgDLK/sgLZK administration in Myrf$^{\Delta iSox10}$ mice ($p = 0.0184$).

(G) There is a reduction in the number of cleaved-caspase-3+ cells within the GCL following sgDLK/sgDLK administration in Myrf$^{\Delta iSox10}$ mice ($p = 0.0254$).

(H) There is a reduction in the number of cleaved-caspase-3+ cells within the GCL following sgDLK/sgLZK administration in Myrf$^{\Delta iSox10}$ mice ($p = 0.0125$).

Scale bars are 500 µm in (D) and 50 µm in (B) and (C). Connected lines indicate retinae from the same mouse in (E) – (H). Paired student's t-test with Šidák's-Bonferroni correction.

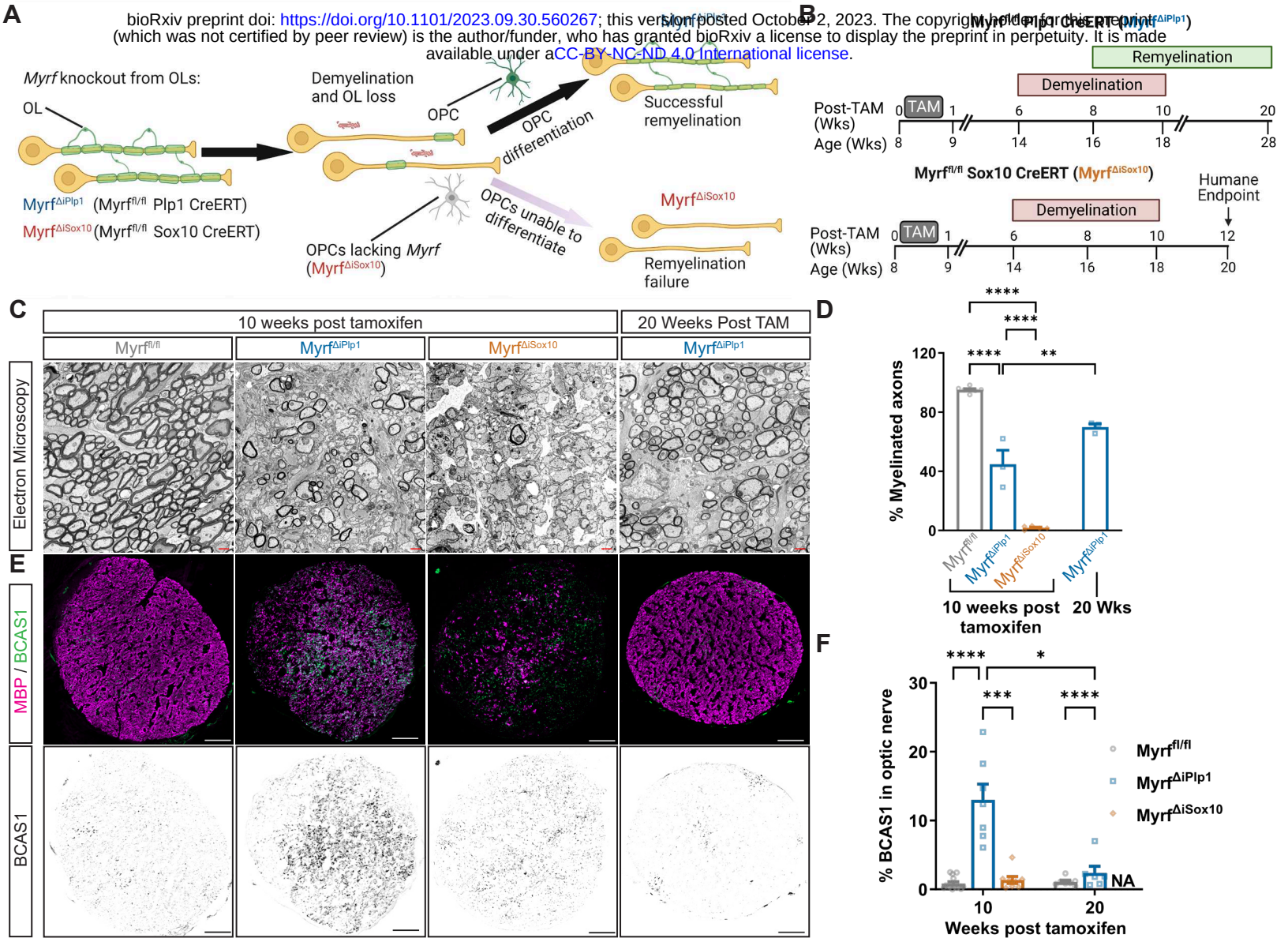

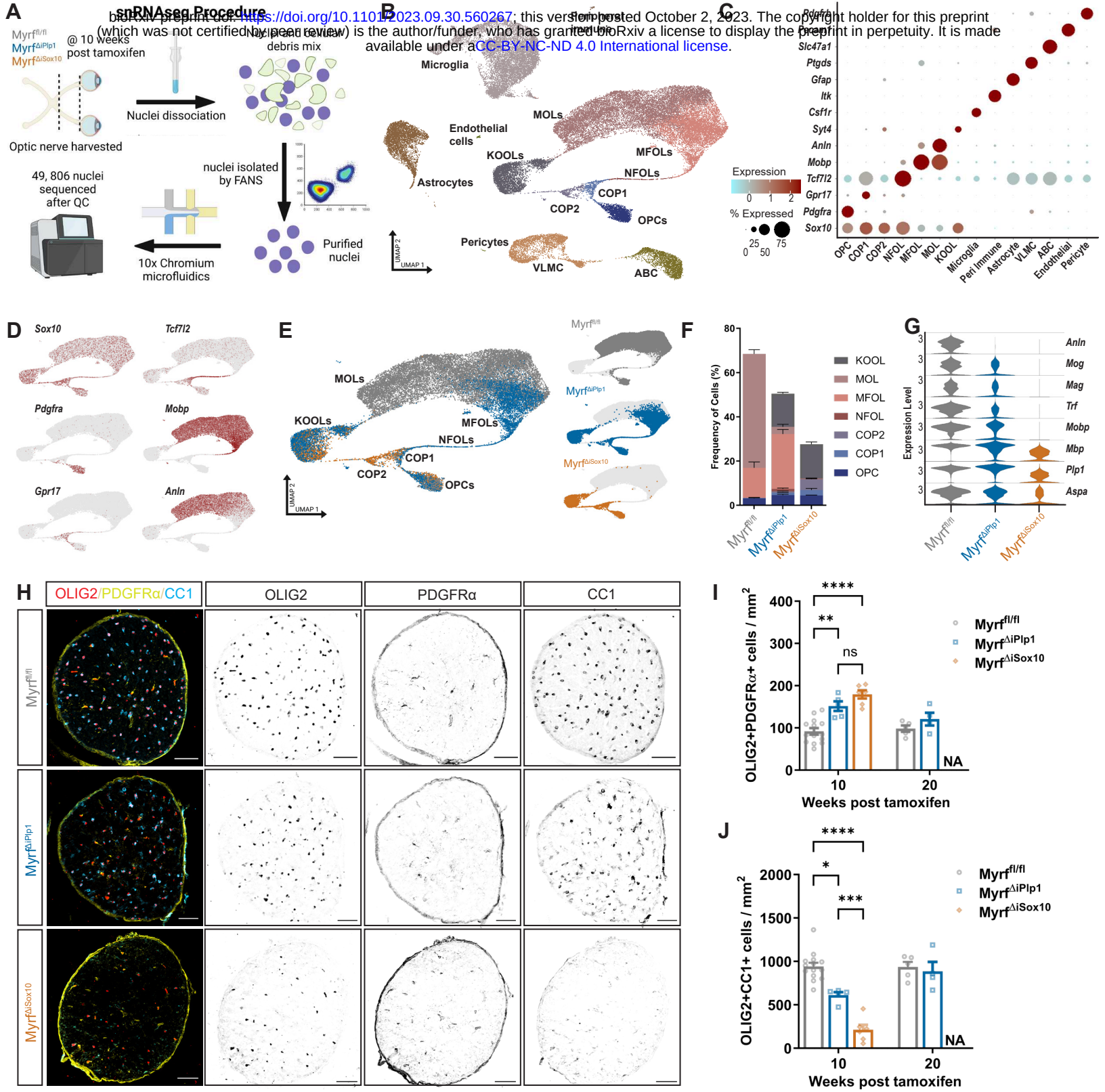

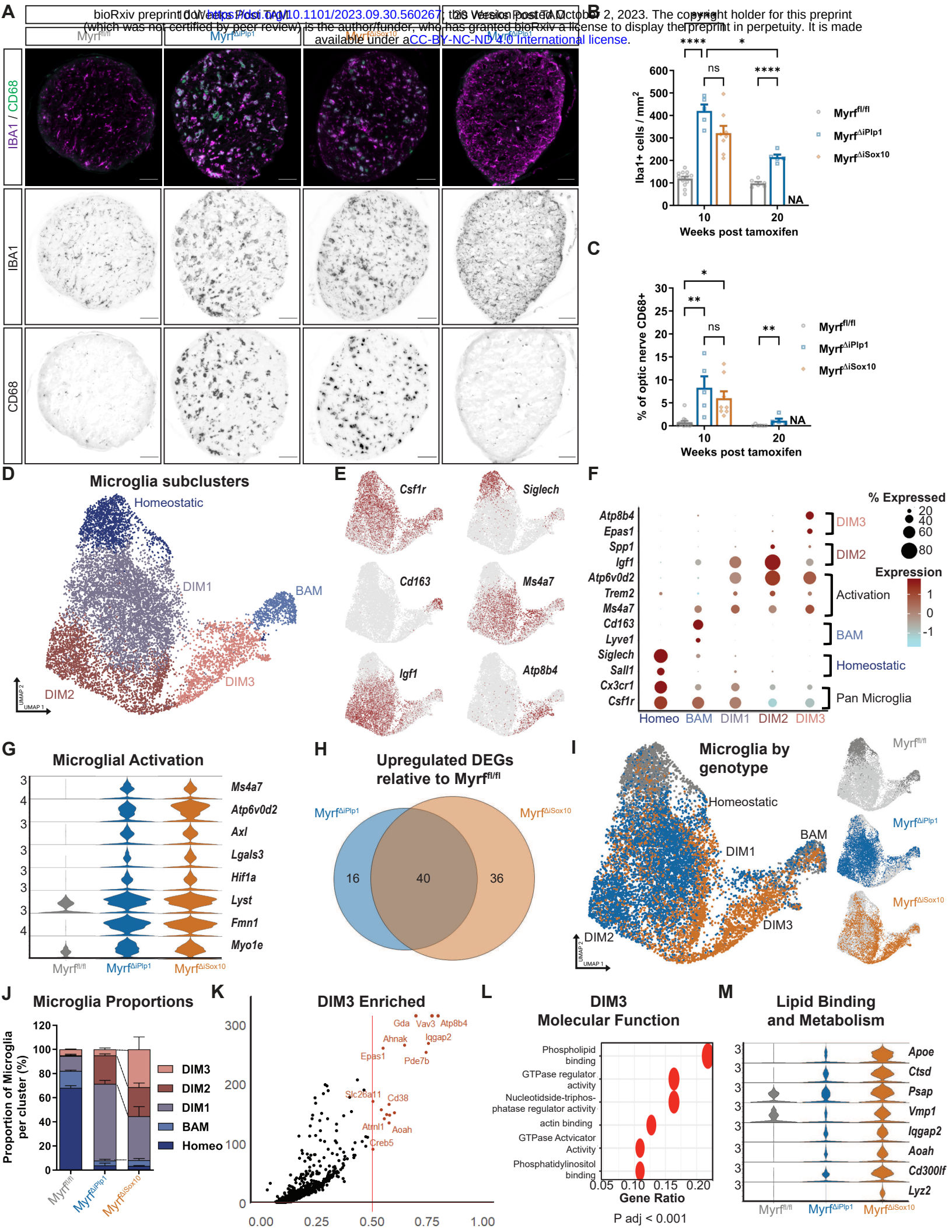

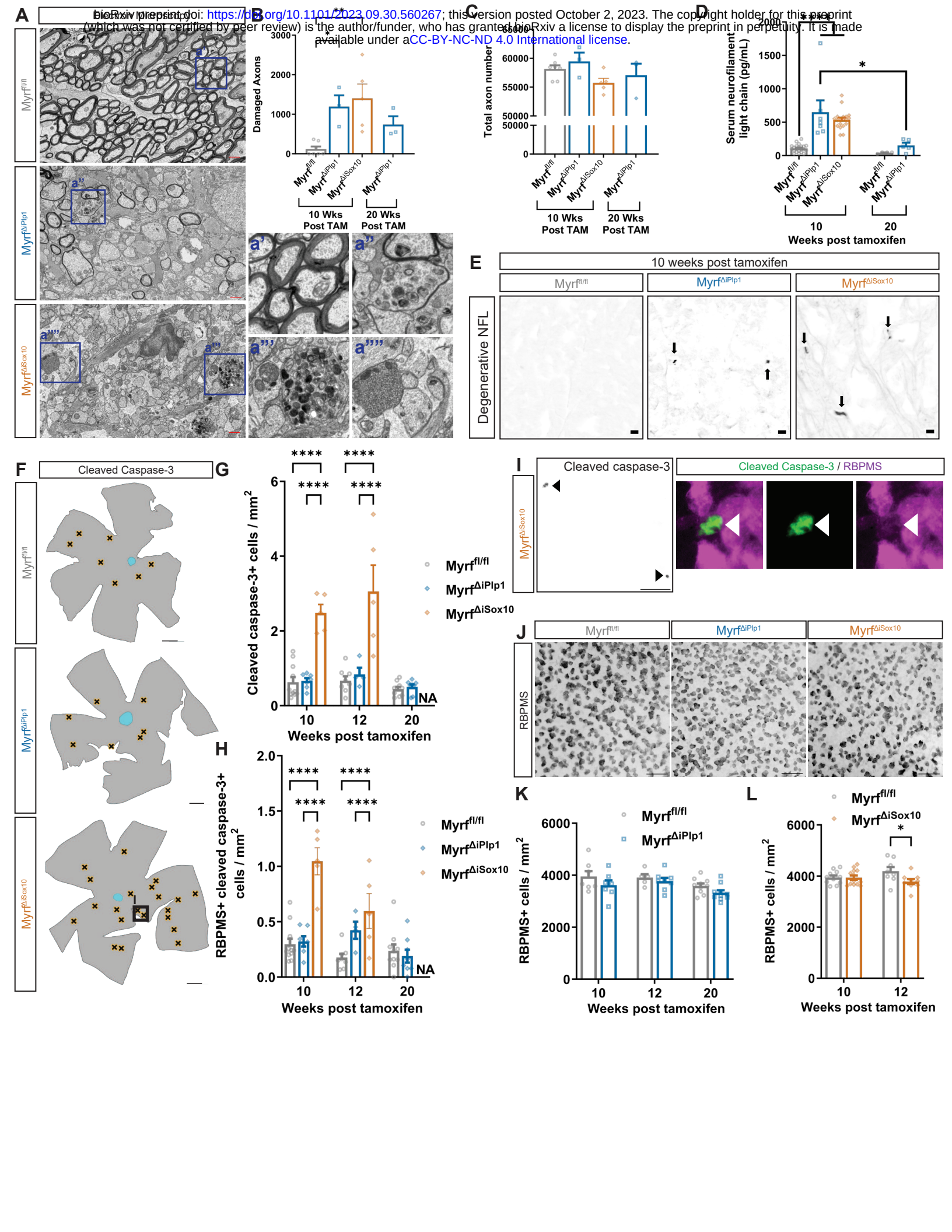

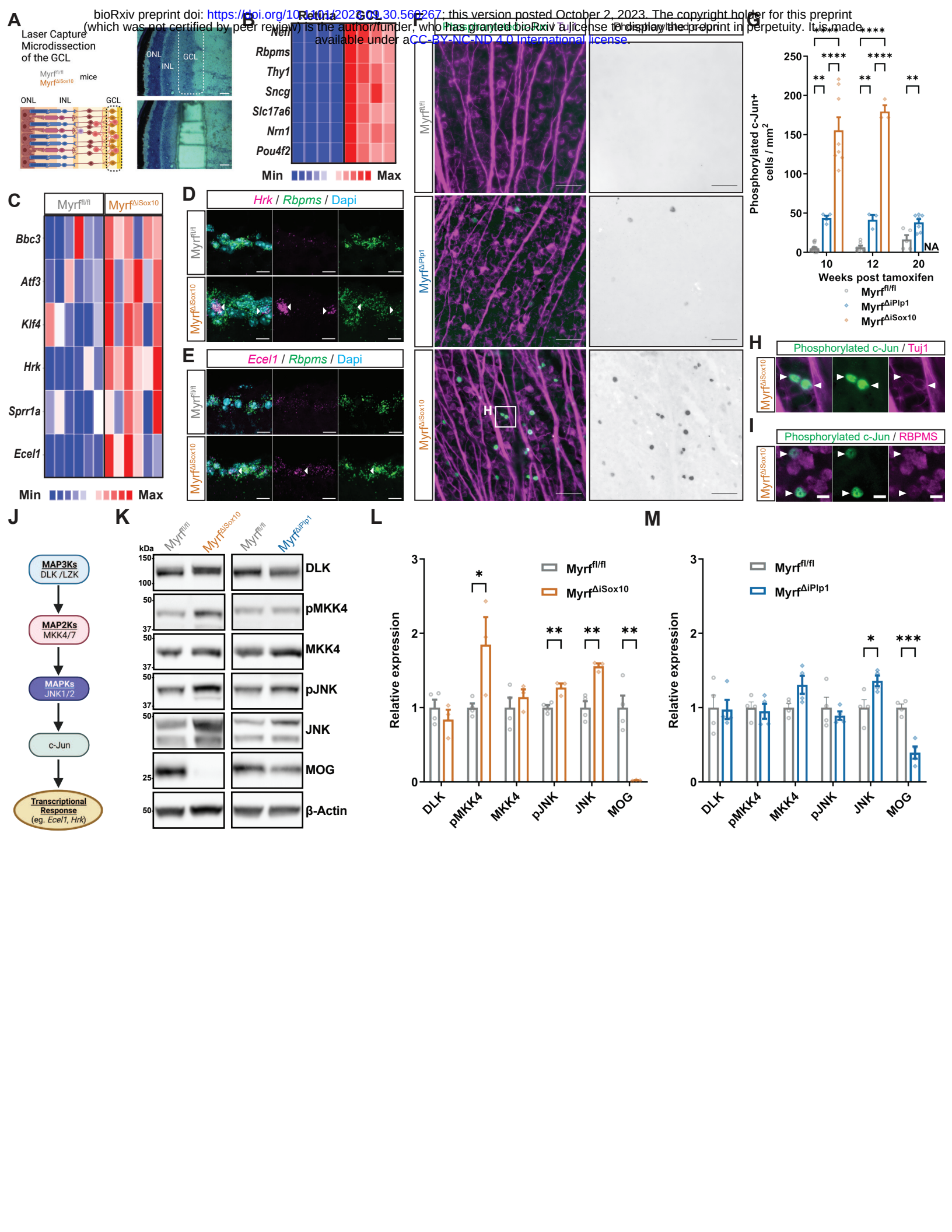

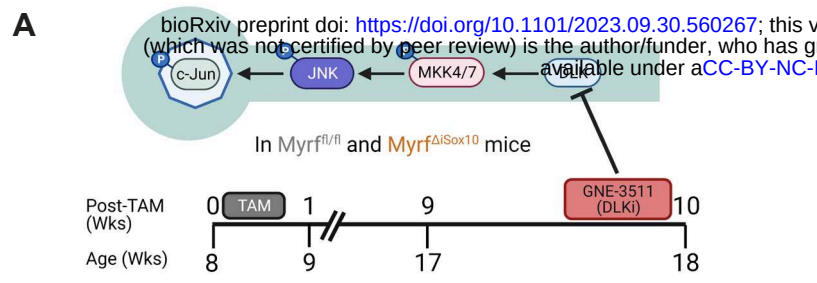

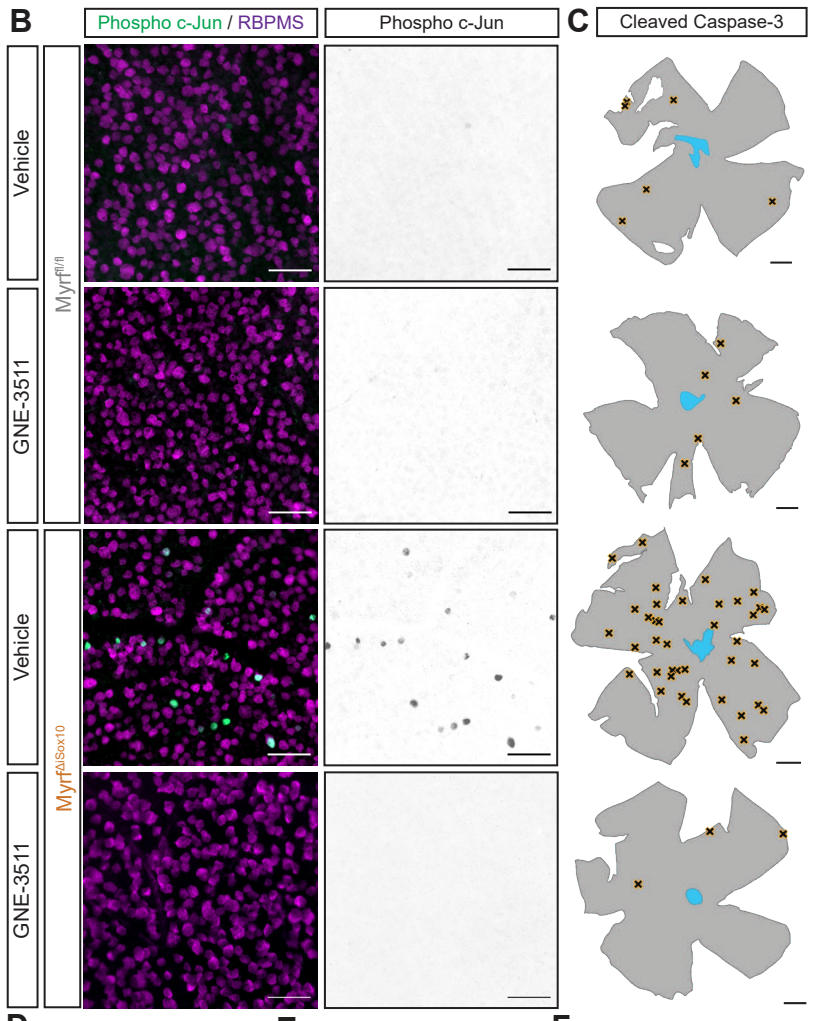

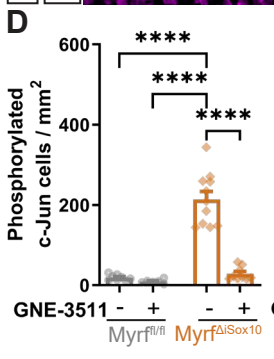

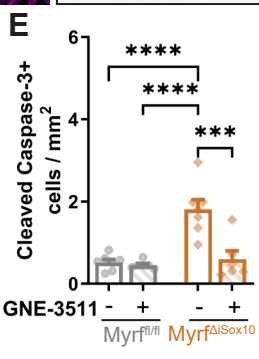

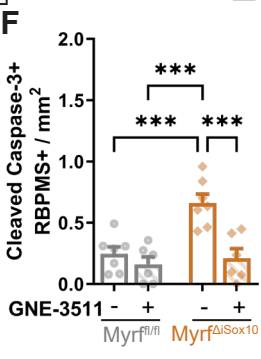

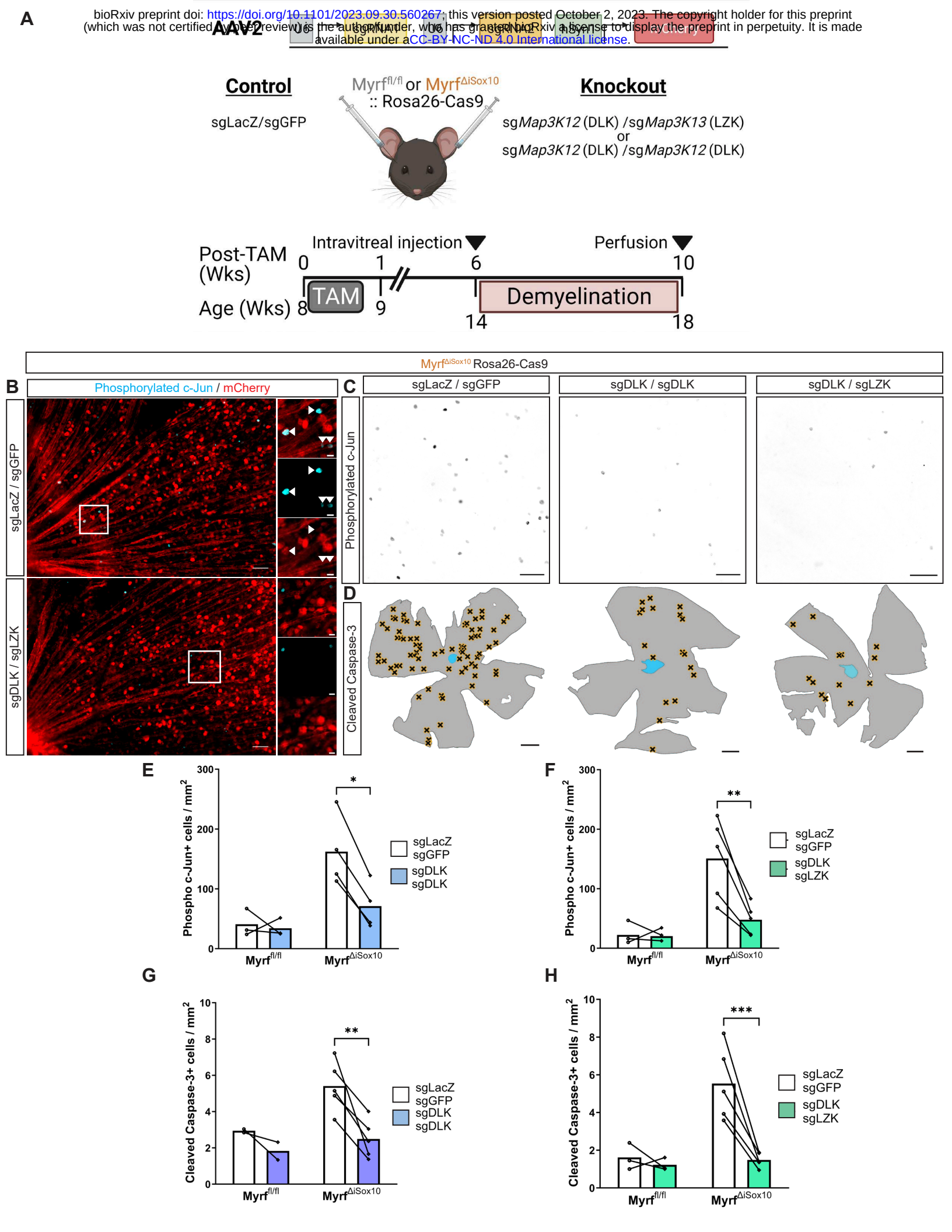

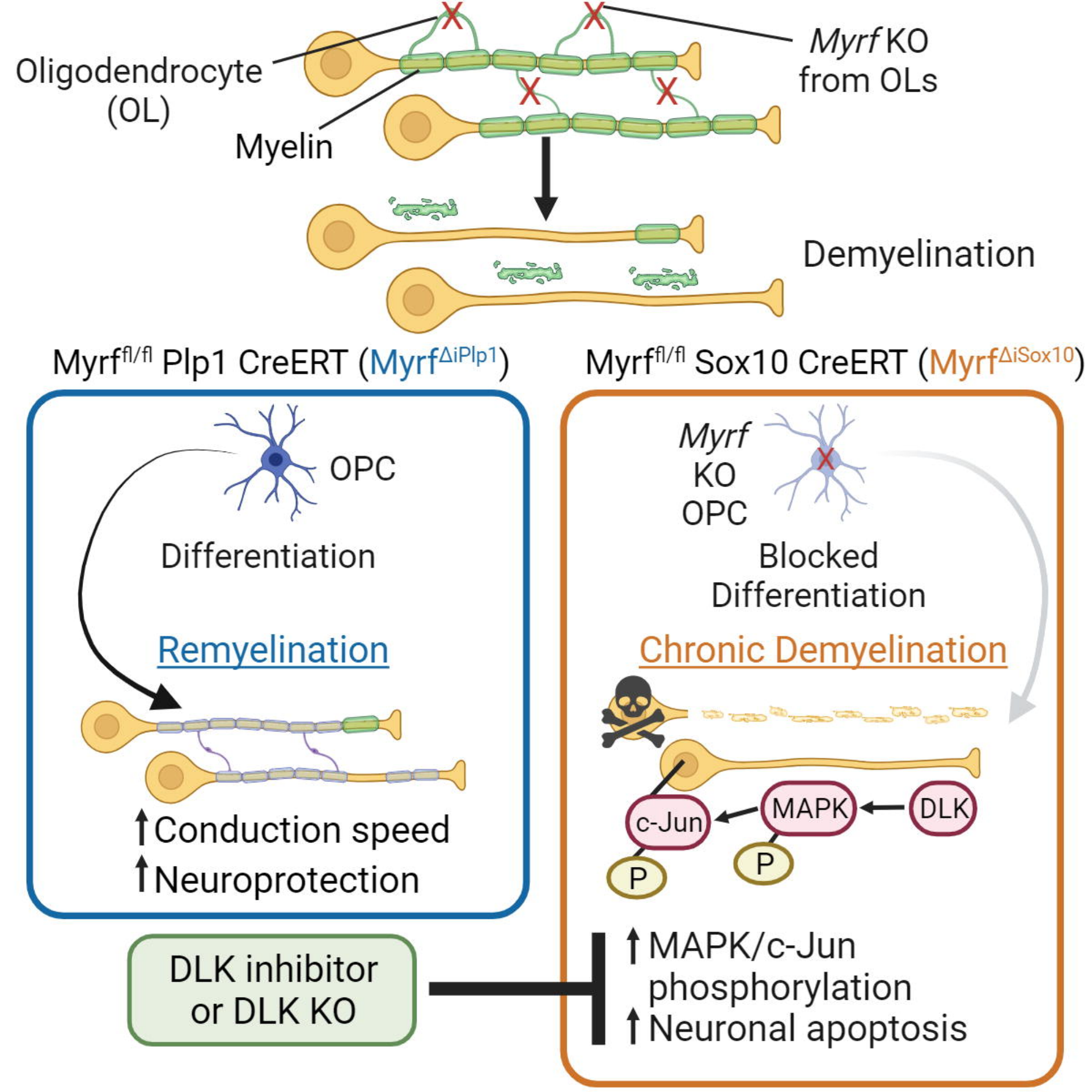
Oligodendrocyte (OL)
Myelin
Myrf KO from OLs
Demyelination
Myrf^fl/fl Plp1 CreERT (Myrf^ΔiPlp1)
OPC
Differentiation
Remyelination
↑Conduction speed
↑Neuroprotection
Myrf^fl/fl Sox10 CreERT (Myrf^ΔiSox10)
Myrf KO OPC
Blocked Differentiation
Chronic Demyelination
c-Jun
MAPK
DLK
P
P
DLK inhibitor or DLK KO
↑MAPK/c-Jun phosphorylation
↑Neuronal apoptosis